Compressible lattice Boltzmann method with rotating overset grids

H. Yoo,[*] G. Wissocq, J. Jacob ⊙, J. Favier ⊙, and P. Sagaut

Aix-Marseille University, CNRS, Centrale Marseille, M2P2, France

The numerical instability of the lattice Boltzmann method (LBM) at high Mach or high Reynolds number flow is well identified, and it remains a major barrier to its application in more complex configurations such as moving geometries. This work combines the compressible lattice Boltzmann model with rotating overset grids (the so-called Chimera method, sliding mesh, or moving reference frame) for high Mach flows. This paper proposes to use the compressible hybrid recursive regularized collision model with fictitious forces (or inertial forces) in a noninertial rotating reference frame. Also, polynomial interpolations are investigated, which allow fixed inertial and rotating noninertial grids to communicate with each other. We suggest a way to effectively couple the LBM with the MUSCL-Hancock scheme in the rotating grid, which is needed to account for thermal effect of compressible flow. As a result, this approach is demonstrated to have an extended Mach stability limit for the rotating grid. It also demonstrates that this complex LBM scheme can maintain the second-order accuracy of the classic LBM by appropriately using numerical methods like polynomial interpolations and the MUSCL-Hancock scheme. Furthermore, the method shows a very good agreement on aerodynamic coefficients compared to experiments and the conventional finite-volume scheme. This work presents a thorough academic validation and error analysis of the LBM for simulating moving geometries in high Mach compressible flows.

I. INTRODUCTION

Over the last three decades, the dawn of the lattice Boltzmann method (LBM) for computational fluid dynamics (CFD) has arrived due to its automatic mesh generation and a low computational cost, leading to high-fidelity simulations for industrial applications. One of the remaining challenges is maintaining its stability and accuracy for high Reynolds and compressible flows, which is now the purpose of ongoing efforts by the LBM community [1–3].

Yet there still remain a number of open issues to enable accurate LBM simulations for industrial applications. One of them is to prove its capability to simulate moving geometries for high Reynolds and compressible flows. Moving geometries represent crucial configurations in aeronautical industry such as rotors, turbofans, and different fluid-structure interaction problems. However, it involves a complex numerical setup for which very different approaches can be found in the literature. The overset grids (the so-called Chimera mesh, sliding mesh, or moving reference frame) simultaneously use fixed and moving meshes with different reference axes [4,5]. The immersed boundary method (IBM) allows one to account for moving geometries by imposing volume forces on moving boundaries. This method is versatile and remains valid for arbitrary motions, but it suffers from a first-order accuracy [6,7]. The arbitrary Lagrange and Eulerian (ALE) method, based on morphing or shifting the mesh to move geometries, requires a large number of interpolations, especially when complex motions are involved [8,9]. Hence, simulating moving geometries in compressible flow is still left as a challenging topic in CFD, not to mention in the LBM.

Therefore, only limited approaches have been used so far in LBM to simulate moving geometries for high Mach number flows. Zhou *et al.* [10] adopted the lattice Boltzmann flux solver (LBFS), which solved the finite-volume based Navier-Stokes equations at each time and space coordinate instead of the LBM scheme, to simulate a turbomachinery flow. The authors state that LBFS was adopted to overcome the numerical complexity coming from coupling the Coriolis force with the LBM in the rotating reference frame. Hejranfar *et al.* [9] applied a similar finite-volume based approach instead of the LBM, referred to as a finite volume lattice Boltzmann solver (FVLBM). In the context of the LBM, Saadat *et al.* [11] coupled the LBM with the ALE method and successfully validated the results up to midrange Mach numbers (Ma < 0.2). Their ALE method morphed an unstructured mesh to actualize the pitching movement. Bhadauria *et al.* [12] conducted a similar approach for fluid-structure interactions and demonstrated its applicability for the same Mach number range (Ma < 0.2).

This work focuses on rotating geometries for high Mach compressible flows, where rotating motion is considered due to an overset grid method (the so-called Chimera method, sliding meshes, or moving reference frame). The overset method has been academically investigated in the LBM for athermal flows only, i.e., without considering the heat equation [4,5,13–15]. Zhang *et al.* [4] first suggested applying the Bhatnagar-Gross-Krook LBM model in the rotating overset grids. Far *et al.* [13] and Lallemand *et al.* [14] studied advanced collision models in the rotating overset grids, such as the Multiple-Relaxation-Time model and cumulant lattice Boltzmann model, but only in the low Mach and laminar flow. Recently Yoo *et al.* [5] employed the HRR model with the rotating overset grids in turbulent flow but low Mach incompressible flow regime. Romani *et al.* simulated acoustic noise of a full scale rotor using commercial LBM software

―――――――――
[*]heesik.yoo@univ-amu.fr

PowerFLOW, but their compressible flow model and rotating grids algorithm are not detailed [16].

In this work, the pressure-based HRR model is applied in a noninertial rotating reference frame. This pressure-based HRR model successfully proved its ability to simulate turbulent high Mach compressible flows in three dimensions [1,2], but has not been tested for moving geometries. In the rotating region, a fictitious force (or so-called inertial force) is considered at each collision and streaming step of the pressure based HRR model by using the forcing term of Guo [17]. Also, since the rotating overset grids use two different meshes simultaneously, fixed and rotating grids share their information through a polynomial interpolation. On top of that, the compressible model introduces a dimensionless temperature θ, whose evolution is considered via an entropy equation solved by a high-order (Monotonic Upstream-centered Scheme for Conservation Laws) MUSCL-Hancock scheme.

In this context, the first major feature of this work is to describe how to use the compressible pressure-based HRR model in noninertial rotating reference frame. Due to this compressible HRR model, the Mach stability limit of an overset noninertial rotating grid is able to be expanded. Also, the gradient-based quadratic interpolation is investigated in the context of compressible LBM. Then we suggest the higher-order MUSCL-Hancock scheme, which is designed to have reduced coupling error with LBM and optimized in the rotating grids.

As a result, this work demonstrates this complex LBM method can retain the second-order accuracy as of the classic LBM, by properly controlling the error of extra numerical add-ons, such as the MUSCL-Hancock scheme and polynomial interpolations. Finally, the method shows its robustness by comparing its aerodynamic coefficients with other references. To the authors' knowledge, this work is the first approach to validate the LBM on moving geometries at high Mach numbers, among any type of movement such as oscillation, translation, and rotation, including any type of numerical method such as IBM, ALE, and the overset grids.

This article is structured as follows. In Sec. II the algorithm of rotating overset grids coupled with the compressible LBM is described. We propose interpretations for the error sources of rotating overset schemes on the LBM. In Sec. III different numerical validations are conducted from an empty rotating domain to 3D rotating solid geometries.

II. NUMERICAL METHOD

A. Discrete forcing term with the pressure-based hybrid recursive regularized lattice Boltzmann model

The pressure-based HRR LBM is able to simulate high Mach number flows around near-transonic and supersonic regimes [1]. This compressible LBM model successfully proved its capability to simulate compressible flows for industrial applications such as considering the large eddy simulation (LES) turbulence model together with a wall model

[1,2]. The overset rotating grids are composed of two different meshes such as fixed and rotating meshes. In the rotating region, all physical vectors are defined with respect to the non-inertial reference axis. Hence, fictitious forces such as inertial and Coriolis forces need to be considered during the collision and the streaming step. Here we couple the pressure-based HRR model with the discrete forcing term F_i to include the fictitious forces. More details are provided in Appendix C. The collision and streaming algorithm reads

$$
\begin{aligned}
f_i(\boldsymbol{x} + \boldsymbol{c}_i \Delta t, t_n + \Delta t) \\
= f_i^{\mathrm{eq}}(\boldsymbol{x}, t_n) + \left(1 - \frac{\Delta t}{\tau}\right) \tilde{f}_i^{\mathrm{neq,HRR}}(\boldsymbol{x}, t_n) \\
+ \frac{1}{2} F_i(\boldsymbol{x}, t_n) + \frac{1}{2} \Psi_i(\boldsymbol{x}, t_n),
\end{aligned}
\tag{1}
$$

where f_i refers to discretized distribution functions depending on space $\boldsymbol{x}$, time t_n and i indicating the velocity discretization index. Regarding this discretization, the D3Q19 lattice [18], composed of velocities $\boldsymbol{c}_i$, is considered. τ is the relaxation time and is related to the fluid viscosity by the relation $\tau = \frac{\mu}{\rho c_s^2} + \frac{\Delta t}{2}$, where μ is the dynamic viscosity, Δt is the time step, ρ is the density, and $c_s = 1/\sqrt{3}$ is the characteristic lattice speed. F_i is the discrete forcing term for fictitious forces, and Ψ_i is a Mach-related correction term, which will be more detailed hereafter. For an in-depth description and analysis of the lattice discretization process and relaxation mechanisms, the reader can refer to Refs. [1,19].

Macroscopic variables, involved in the definitions of functions such as f_i^{eq}, F_i, and Ψ_i, are computed as

$$
\rho(\boldsymbol{x}, t_n) = \sum_i f_i(\boldsymbol{x}, t_n) + \rho(\boldsymbol{x}, t_{n-1})[1 - \theta(\boldsymbol{x}, t_{n-1})], \tag{2}
$$

$$
\rho\boldsymbol{u}(\boldsymbol{x}, t_n) = \sum_i \boldsymbol{c}_i f_i(\boldsymbol{x}, t_n) + \frac{\Delta t}{2} \boldsymbol{F}(\boldsymbol{x}, t_n) + O_{\mathrm{LBM}}(\Delta t^2), \tag{3}
$$

where θ refers to the dimensionless temperature $\theta = T/T_{\mathrm{ref}}$ which is computed from the entropy equation. More details are provided in Secs. II B and II C. The fictitious force reads

$$
\boldsymbol{F}(\boldsymbol{x}, t_n) = -2\rho\boldsymbol{\omega} \times \boldsymbol{u}(\boldsymbol{x}, t_n) + \rho\boldsymbol{\omega} \times (\boldsymbol{\omega} \times \boldsymbol{r}), \tag{4}
$$

where $\boldsymbol{\omega} = [\omega_1\ \omega_2\ \omega_3]$ is the angular velocity vector of the rotating mesh and $\boldsymbol{r}$ is the vector of coordinates with respect to the rotation center. In Eq. (3) the force $\boldsymbol{F}(\boldsymbol{x}, t_n)$ includes the Coriolis force, which is a function of velocity. As a consequence, the computation of the velocity $\boldsymbol{u}(\boldsymbol{x}, t_n)$ given by Eq. (3) is implicit. Hence, it is needed to define the fictitious force $\boldsymbol{F}(\boldsymbol{x}, t_n)$ considering this implicit character. There are different ways to deal with this issue, which handle this problem by using either algebraic operations or time-splitting operators [20,21]. The present work algebraically solves the fictitious force at the current time step. By substituting (3) into (4), the force is represented as a function of all the known values as

$$
\boldsymbol{F}(t_n) = \begin{bmatrix} 1 & -\Delta t\omega_3 & \Delta t\omega_2 \\ \Delta t\omega_3 & 1 & -\Delta t\omega_1 \\ -\Delta t\omega_2 & \Delta t\omega_1 & 1 \end{bmatrix}^{-1} \left[-2\boldsymbol{\omega} \times \sum_i \boldsymbol{c}_i f_i(t_n) + \rho\boldsymbol{\omega} \times (\boldsymbol{\omega} \times \boldsymbol{r}) + O_{\mathrm{LBM}}(\Delta t^2) \right]. \tag{5}
$$

This computed fictitious force is then applied to define macroscopic velocity in Eq. (3). Furthermore, the calculated fictitious force has to be imposed during the collision and streaming step as given by Eq. (1) through the discrete forcing term F_i. The solution proposed by Guo is used here [17]. To comply with the pressure-based HRR collision model (1), it reads

$$F_i = w_i \left[\frac{\boldsymbol{c}_i - \boldsymbol{u}}{c_s^2} + \frac{(\boldsymbol{c}_i \cdot \boldsymbol{u})}{c_s^4} \boldsymbol{c}_i \right] \cdot \boldsymbol{F}. \qquad (6)$$

This discrete forcing term can introduce a numerical error [17], which is known to be of second order $O(\Delta x^2)$ [19,22]. This error also depends on the type of discrete forcing scheme such as such as the forcing terms of Guo [17] and He [23]. Suzuki *et al.* demonstrated that the Guo forcing term is able to recover the Navier-Stokes equations more accurately than the He forcing term, when it comes to spatially varying forces [25]. In the context of rotating overset schemes, both forcing terms have been compared, and Guo's forcing term showed better performances [5]. Recently Li *et al.* proposed the higher-order Guo forcing term, which is claimed to be optimized for thermal compressible flow, but in this research we choose the standard second-order Guo forcing term [24].

$f_i^{\mathrm{eq}}(\boldsymbol{x}, t)$ refers to the equilibrium distribution, expanded here to the third order in $\boldsymbol{c}_i$ as in Refs. [1,2]. The macroscopic density ρ and nondimensional temperature θ which are needed to define the equilibrium function follow the definitions of the pressure-based HRR model [1]. The velocity $\boldsymbol{u}$ is defined including half of the force term as in Eq. (3) [5,17].

$\tilde{f}_i^{\mathrm{neq,HRR}}(\boldsymbol{x}, t)$, the so-called off-equilibrium distribution function, is reconstructed from a macroscopic tensor denoted as $a_{\alpha\beta}^{\mathrm{neq,HRR}}$. This step is known as regularization [26,27]. The definition of the off-equilibrium tensor $a_{\alpha\beta}^{\mathrm{neq,HRR}}$ is provided in Appendix C and Refs. [1,2]. This off-equilibrium tensor can be computed either from the off-equilibrium distribution function ($a_{\alpha\beta}^{\mathrm{neq,}LBM}$) or from the shear stress $\nabla \boldsymbol{u}$ computed by finite differences ($a_{\alpha\beta}^{\mathrm{neq,FD}}$) [28]. In the HRR model, these two approaches are hybridized with a parameter σ, defining the ratio between both ways of computing the nonequilibrium tensors:

$$a_{\alpha\beta}^{\mathrm{neq,HRR}} = \sigma a_{\alpha\beta}^{\mathrm{neq,}LBM} + (1 - \sigma) a_{\alpha\beta}^{\mathrm{neq,FD}}. \qquad (7)$$

Unless otherwise mentioned, σ is set to unity in this work, meaning that the finite difference part is not used.

The simulation of high Mach number flows with the standard LBM is known to result in a deviation with the Navier-Stokes equations referred to as the Galilean invariant error [29–31]. The body-force term Ψ_i is designed to address this error. This correction term includes the aforementioned macroscopic values ρ, $\boldsymbol{u}$, θ and their gradients. In this research, the high Mach error term is considered to be same formulation as in the inertial frame. The derivation step of the high Mach error in the noninertial frame is described in Appendix E. More details about this correction term for the pressure-based HRR are described in Refs. [1,2].

B. Compressible LBM: θ and independent Courant-Friedrichs-Lewy number

Apart from the standard athermal LBM, the compressible LBM includes a macroscopic parameter θ, which is the nondimensional temperature. One interesting point of this parameter is that it enables the compressible LBM to freely modify its Courant-Friedrichs-Lewy (CFL) number defined as [32]

$$\mathrm{C_{CFL}} = \frac{|u| + c}{\Delta x / \Delta t} = c_s^*(1 + \mathrm{Ma}), \qquad (8)$$

where c is the sound speed and c^* is its dimensionless form (nondimensionalized by $\Delta x / \Delta t$). In the conventional athermal LBM, the CFL number is constrained as a linear function of the Mach number because the dimensionless sound speed is constant:

$$c_{ath}^* = \frac{\sqrt{r_{\mathrm{gas}} T_{\mathrm{ref}}}}{\Delta x / \Delta t} = \frac{1}{\sqrt{3}}, \qquad (9)$$

where r is the gas constant. This prevents the athermal LBM from reaching high Mach number due to the CFL limitation. However, in the compressible LBM model, the dimensionless speed of sound c^* is defined with respect to the dimensionless temperature θ [Eq. (10)] as

$$c_{th}^* = \frac{\sqrt{\gamma r_{\mathrm{gas}} T}}{\Delta x / \Delta t} = \frac{\sqrt{r_{\mathrm{gas}} T_{\mathrm{ref}}}}{\Delta x / \Delta t} \sqrt{\gamma \frac{T}{T_{\mathrm{ref}}}} = \frac{1}{\sqrt{3}} \sqrt{\gamma \theta}, \qquad (10)$$

where γ is the heat capacity ratio. Therefore, the compressible LBM can reach higher Mach flow without violating the CFL condition by modifying the parameter θ.

C. The MUSCL-Hancock scheme for entropy equation

As discussed above, the evolution of the dimensionless temperature θ is solved via the entropy equation, which reads

$$\frac{\partial s}{\partial t} + u_\alpha \frac{\partial s}{\partial \alpha} = -\frac{1}{\rho T} \frac{\partial q_\alpha}{\partial \alpha} + \frac{\sigma_{\alpha\beta}}{\rho T} \frac{\partial u_\alpha}{\partial \beta}, \qquad (11)$$

where an implicit summation is done over indices $\alpha, \beta \in \{x, y, z\}$, and the entropy s is defined as

$$s = \frac{r}{\gamma - 1} \ln\left(\frac{r_{\mathrm{gas}} T_{\mathrm{ref}} \theta}{\rho^{\gamma-1}} \right), \qquad (12)$$

where $q_\alpha = -\lambda \partial T / \partial \alpha$ is the heat flux, λ is the heat conductivity, and $\sigma_{\alpha\beta} = -a_{\alpha\beta}^{\mathrm{neq,HRR}}$ is the shear stress tensor. The right-hand-side terms of Eq. (11), namely, the heat flux and the viscous heating, are discretized using a standard finite-difference scheme as suggested in [1]. In this section the focus is put on the way the convective term is computed, and more precisely the entropy flux $u_\alpha \partial s / \partial \alpha$ using a MUSCL-Hancock scheme. For this purpose and for the sake of simplicity, diffusive terms will not be written in the equations below.

The entropy equation is nonconservative compared to the energy equation. However, it is commonly preferred for stability purposes since it is a simple advection-diffusion equation. This entropy equation allows one to predict entropy at the next time step by using spatial fluxes at the current time step, and a high-order precision can be preserved using the MUSCL-Hancock scheme [33,34]. Solving the entropy equation

(or energy equation) is necessary to consider compressible flow, but it can yield more dissipation to the numerical scheme since it is an add-on to the original LBM equation. Hence, we choose the high-order MUSCL-Hancock scheme to minimize this dissipation error originating from the coupling between the LBM and entropy equation. This scheme guarantees the second- or third-order precision in time by predicting an entropy scalar after half a time step.

Here we would like to underline two characteristics of the fluxes in the rotating overset grids: they are multidirectional and coupled with the LBM. First, the rotating overset grids encounter fluxes in any direction according to rotation angle. This implies that considering the multidirectionality of the MUSCL-Hancock scheme is crucial for rotating overset grids. This multidirectionality can be considered by including diagonal fluxes. In addition, the LBM part is used to compute ρ and u, while the MUSCL-Hancock scheme is used to compute temperature θ. Depending on the way it receives velocity information from LBM, the coupling gives different order of numerical error. Given that coupling with different equations is required for LBM to simulate multiphysics, the demonstration here can assist in understanding how to couple LBM with other equations such as managing their coupling error and maintaining sufficient accuracy. In this context, we suggest the third-order unsplit MUSCL-Hancock scheme to deal with the above two issues. In this work, an original higher-order MUSCL-Hancock scheme is proposed by addressing the two points mentioned above. It will be referred to as MUSCL $- 2D - \phi_{n+1/2}$. This scheme is compared with the MUSCL-Hancock scheme proposed in a previous work [1], referred to as MUSCL $- 1D - \phi_n$.

First, the coupling error between LBM and the MUSCL-Hancock scheme is considered when the spatial fluxes are evaluated. The entropy scheme proposed by Farag $et\ al.$ [1] reads

$$\frac{s(\boldsymbol{x}, t + \Delta t) - s(\boldsymbol{x}, t)}{\Delta t} + u_\alpha(\boldsymbol{x}, t) \frac{F_{+\Delta\alpha/2}(\boldsymbol{x}, t) - F_{-\Delta\alpha/2}(\boldsymbol{x}, t)}{\Delta x}$$
$$= 0, \tag{13}$$

where $F_{+\Delta\alpha/2}$ and $F_{-\Delta\alpha/2}$ are fluxes at the border of the cell in the direction α, whose expressions will be provided hereafter. Note that one systematically has by definition $F_{-\Delta\alpha/2}(\boldsymbol{x}, t) = F_{+\Delta\alpha/2}(\boldsymbol{x} - \boldsymbol{e}_\alpha \Delta x, t)$, where $\boldsymbol{e}_\alpha$ is the unit vector in the direction α.

As demonstrated in Appendix A, this can lead to a third-order accuracy $O(\Delta t^3)$ on the entropy equation when u_α is constant. However, the accuracy is degraded to the first-order $O(\Delta t)$ when it comes to nonconstant flows. Its low accuracy can be more severe as the velocity u_α varies with time. Therefore, it is suggested to evaluate the velocity after half a time step $u_\alpha(\boldsymbol{x}, t + \Delta t/2) = [u_\alpha(\boldsymbol{x}, t + \Delta t) + u_\alpha(\boldsymbol{x}, t)]/2$ to compute the fluxes, which yields a second-order accuracy $O(\Delta t^2)$ even for nonconstant flows:

$$\frac{s(\boldsymbol{x}, t + \Delta t) - s(\boldsymbol{x}, t)}{\Delta t} + u_\alpha(\boldsymbol{x}, t + \Delta t/2)$$
$$\times \frac{F_{+\Delta\alpha/2}(\boldsymbol{x}, t) - F_{-\Delta\alpha/2}(\boldsymbol{x}, t)}{\Delta x} = 0. \tag{14}$$
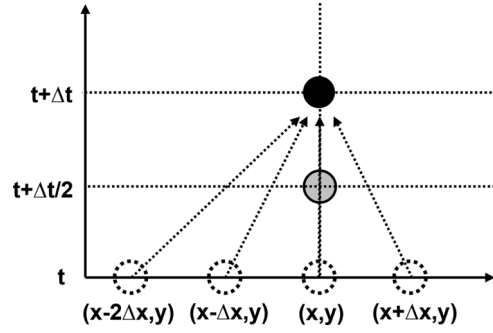

FIG. 1. Stencil of the MUSCL-Hancock scheme for unsteady flux: a target point (filled circle), points at the current time step (dashed line circle), and point after the half time step for unsteady flow (gray circle). For simplicity, the stencil is described for the $u_x > 0$ and $u_y = 0$ case.

This newly added point $u_\alpha(\boldsymbol{x}, t + \Delta t/2)$ in the time axis is shown in Fig. 1. More details about its order of accuracy are provided in Appendix A.

Moreover, the multidirectional scheme is proposed by considering the diagonal terms while predicting the scalar values $F_{+\Delta\alpha/2}(\boldsymbol{x}, t)$ and $F_{-\Delta\alpha/2}(\boldsymbol{x}, t)$. There are different ways to consider multidirectional fluxes, such as the splitting method [34]. However, the splitting method requires double time loops in two dimensions and six time loops in three dimensions [34]. Therefore, this work adopts an unsplit method which does not need multiloops, but uses diagonal entropy and velocity components instead, which are easily accessible for the case of Cartesian grids. The midcell flux is defined in this case as

$$F_{+\Delta\alpha/2}(\boldsymbol{x}, t) = s(\boldsymbol{x}, t) + \frac{1}{2} \Delta_\alpha(\boldsymbol{x}, t)$$
$$- \sum_{\beta \in \{x,y,z\}} \frac{u_\beta}{2} \frac{\Delta t}{\Delta x} \Delta_\beta(\boldsymbol{x}, t), \tag{15}$$

where Δ_α refers to the MUSCL-Hancock slope in the direction α, which is more detailed in Appendix A. Here Eq. (15) refers to the case where the convection velocity $u_\alpha > 0$. The slope Δ_α has a five-point stencil when the slope is parallel to the flow by which the MUSCL-Hancock scheme can recover the third-order accuracy $O(\Delta x^3)$ on the entropy equation (11) [1,33,34]. On top of that, by adding the slope perpendicular to the flow, the MUSCL-Hancock scheme can recover the second-order accuracy $O(\Delta x^2)$ on the entropy equation for nonaligned flows [34]. The extended stencils are described in Fig. 2.

Then the predicted entropy fluxes of Eq. (15) are substituted into the entropy equation (14). This yields the MUSCL $- 2D - \phi_{n+1/2}$ scheme, which reads

$$s(\boldsymbol{x}, t + \Delta t) = s(\boldsymbol{x}, t) + \sum_{\alpha \in \{x,y,z\}} u_\alpha(\boldsymbol{x}, t + \Delta t/2)$$
$$\times \frac{\Delta t}{\Delta x} [F_{-\Delta\alpha/2}(\boldsymbol{x}, t) - F_{\Delta\alpha/2}(\boldsymbol{x}, t)]$$
$$+ \begin{cases} O(\Delta x^3, \Delta t^3), & \text{if 1D and } u_\alpha \text{ is constant} \\ O(\Delta x^2, \Delta t^2), & \text{otherwise.} \end{cases}$$
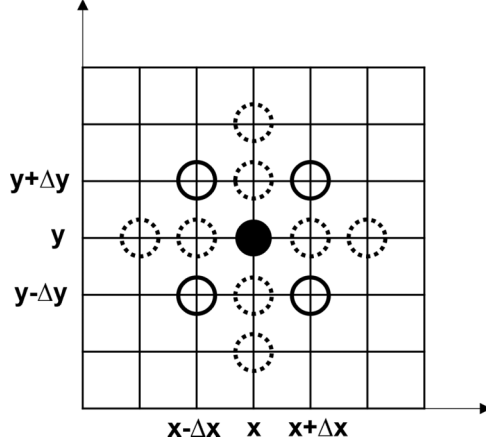$$\tag{16}$$

FIG. 2. Stencil of the multidirectional MUSCL-Hancock scheme. A target point (filled circle), points for 1D flow (dashed line circle) and diagonal points for multidirectional flux (solid line circle).

This scheme guarantees a second-order accuracy $O(\Delta x^2)$ for multidirectional flows, and a third-order accuracy $O(\Delta x^3)$ for constant and unidirectional flows. Details on the accuracy are provided in Appendix A.

Note that without considering the multidirectionality, the MUSCL-Hancock scheme predicts the entropy flux by

$$\bar{F}_{+\Delta\alpha/2}(\boldsymbol{x}, t) = s(\boldsymbol{x}, t) + \left(\frac{1}{2} - \frac{u_\alpha}{2} \frac{\Delta t}{\Delta x} \right) \Delta_\alpha(\boldsymbol{x}, t), \qquad (17)$$

for a convection velocity $u_\alpha > 0$. This unidirectional flux yields

$$
\begin{aligned}
&s(\boldsymbol{x}, t + \Delta t) \\
&= s(\boldsymbol{x}, t) + \sum_{\alpha \in \{x,y,z\}} u_\alpha(\boldsymbol{x}, t + \Delta t/2) \\
&\quad \times \frac{\Delta t}{\Delta x}[\bar{F}_{-\Delta\alpha/2}(\boldsymbol{x}, t) - \bar{F}_{\Delta\alpha/2}(\boldsymbol{x}, t)] \\
&= \begin{cases} O(\Delta x^3, \Delta t^3), & \text{if 1D and } u_\alpha \text{ is constant} \\ O(\Delta x^2, \Delta t^2), & \text{if 1D and } u_\alpha \text{ is nonconstant} \quad (18) \\ O(\Delta x, \Delta t), & \text{otherwise.} \end{cases}
\end{aligned}
$$

The unidirectional MUSCL-Hancock scheme can still give a third-order accuracy for constant and unidirectional flows, but the accuracy goes down to the first order in multidirectional flows. The accuracy orders of the uni- and multidimensional MUSCL-Hancock schemes with and without half-time interpolation are summarized in Table I.

D. Interpolation between rotating and fixed grids

In the overset scheme, both fixed and rotating grids exist simultaneously as exchanging their information at the borders (see Fig. 3). The border nodes receive the macroscopic values $(\rho, \boldsymbol{u}, a_{\alpha\beta}^{\text{neq}}, \theta)$ from the surrounding nodes in another region, through a polynomial interpolation (see Fig. 4). The gradient-based quadratic interpolation is applied for ρ, $\boldsymbol{u}$ and θ, which has a third-order accuracy in space [5,35]. At the borders, the distribution functions f_i^{eq}, f_i^{neq} are reconstructed from the interpolated macroscopic values, and then the collision and streaming steps are performed. On top of that, the interpolated macroscopic values are put into the entropy equation at the boundaries to transport θ. More details about the interpolation algorithm are provided in Appendixes B and D and Ref. [5].

In terms of the interpolation, this work delivers the significance of quadratic interpolation having the third-order accuracy $O(\Delta x^3)$. It is higher than the accuracy of base LBM $O(\Delta x^2)$ so that the interpolation does not ruin physics of LBM [36]. Moreover, this aspect may imply the possibility that the quadratic interpolation is optimum for LBM applications compared to the higher-order interpolation like the cubic interpolation. Also, to take into account large pressure gradients of compressible flow, we expand the quadratic interpolation to the pressure variables such as (ρ, θ), apart from velocities $\boldsymbol{u}$.

III. NUMERICAL VALIDATION

In all the cases introduced in this section, the MUSCL $- 2D - \phi_{n+1/2}$ scheme is considered for the entropy equation, unless otherwise stated.

A. Vortex advection

The advection of a vortex is tested over the rotating overset grids. The purpose of this test case is to identify how long the vortex structure can be sustained as it flows through the periodic domain. Inviscid vortex structure can be conserved as being advected on a single fixed grid in compressible flow [1]. Here the higher-order MUSCL-Hancock scheme with diagonal terms and the flux after a half time step is applied (MUSCL $- 2D - \phi_{n+1/2}$). The Guo forcing term is selected to impose the fictitious forces, and the gradient-based quadratic interpolation is chosen. The vortex is initialized by

$$u_x = u_0 - \epsilon \left(\frac{y - y_0}{R} \right) \exp \left[-\frac{(x - x_0)^2 + (y - y_0)^2}{2R^2} \right],$$

TABLE I. Accuracy orders in space and time of the different MUSCL-Hancock schemes according to the considered type of flow.

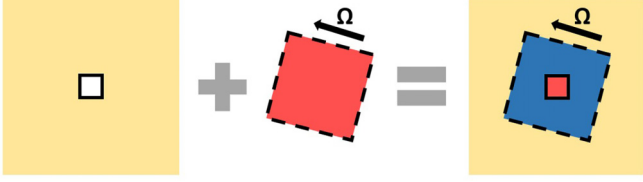| Type of flow	$MCL - 1D - \Phi_n$	$MCL - 1D - \phi_{n+1/2}$	$MCL - 2D - \phi_n$	$MCL - 2D - \phi_{n+1/2}$
1D flow, $\boldsymbol{u}$ constant	Third order	Third order	Third order	Third order
1D flow, $\boldsymbol{u}$ nonconstant	First order	Second order	First order	Second order
3D flow, $\boldsymbol{u}$ constant	First order	First order	Second order	Second order
3D flow, $\boldsymbol{u}$ nonconstant	First order	First order	First order	Second order

FIG. 3. Schematic diagram of the overset grids: fixed grid (yellow), rotating grid (red), overlapped region (blue), interpolation border from rotating to fixed grid (solid line), and interpolation border from the fixed to rotating grid (dashed line). From [5].

$$u_y = \epsilon \left(\frac{x - x_0}{R} \right) \exp \left[-\frac{(x - x_0)^2 + (y - y_0)^2}{2R^2} \right],$$

$$\rho = \rho_0 \left[1 - \frac{\gamma - 1}{\gamma} \frac{\epsilon^2}{2 r_{gas} T_0} \right.$$

$$\left. \times \exp \left(-\frac{(x - x_0)^2 + (y - y_0)^2}{R^2} \right) \right]^{\frac{1}{\gamma - 1}},$$

$$p = \frac{p_0}{\rho_0^\gamma} \rho^\gamma. \tag{19}$$

The vortex advection speed is $Ma_0 = u_0/c = 0.1$. The vortex strength is set to $\epsilon = 0.15$, which represents the local Mach number at the periphery of the rotating vortex. The viscosity is set to $\mu = 10^{-25}$ for the inviscid condition. The ambient initial density is set to $\rho_0 = 1$ and pressure to $p_0 = 1$; γ is set to 1.4 and $r_{gas} = 1$. More details of the vortex initialization are described in [37,38]. All the test cases of this section adopt 10 points in the radius of the vortex ($R = 10\Delta x$). The number of points in the length of square domain is 200 ($L = 200\Delta x$).

Figure 5 shows that vortex structures are well conserved after five flow-through times $T_{FTT} = cMa_0 t/L$, where L is the channel length. The rotation speed of the overset mesh is given by $Ma_{r\omega} = r\omega/c$, where r is the distance between the rotation center and the corner point of the overset mesh. The CFL number is $C_{CFL}^0 = 0.49$ based on the advection speed Ma_0. The L2 error is compared with the reference as $E = \sqrt{\frac{\Sigma (p - p_{ref})^2}{N}}$, where the reference is the same vortex advection simulation on a single fixed grid and N is the number of mesh nodes. The overset scheme is found to well conserve the

FIG. 5. Cross-sectional pressure profile of advecting vortex over the rotating overset grids at $5T_{FTT}$.

vortex structure, with about 0.001% errors at various rotation speeds.

Figure 6 shows the maximum mesh rotation speeds for various values of the CFL number calculated using the convection velocity $Ma_0 = 0.1$, such as $C_{CFL}^0 = c^*(1 + Ma_0)$. As previously explained, the dimensionless variable θ is used, which is a function of time step Δt, lattice size Δx, and ambient initial temperature T_0. Hence, the CFL number and θ are adjusted by reducing Δt while having constant Δx and T_0. As shown in Fig. 6 the stability limit is expanded from $Ma_{r\omega} = 0.72$ to $Ma_{r\omega} = 1.55$ as reducing the CFL number from the inlet velocity C_{CFL}^0. At each C_{CFL}^0, the stability limit is constrained when the CFL number C_{CFL} based on local velocity $[C_{CFL} = c^*(1 + Ma)]$ reaches its stability limit. On the other hand, the athermal LBM has a unique maximum rotating speed as $Ma_{r\omega} = 0.75$ regardless of time step Δt, where the model is close to its CFL stability limit. At the given inlet Mach number Ma_0, the athermal LBM has unique CFL number $C_{CFL}^0 = c^*(1 + Ma_0)$, which cannot be modified by adjusting the time step because the nondimensional speed of sound is maintained constant regardless of the time step. Hence, the stability limit is defined based on only the local Mach number Ma.
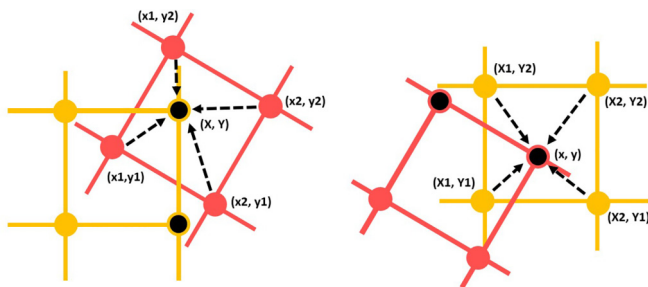

FIG. 4. Schematic diagram of the interpolation between the moving (red or gray in gray scale) and fixed (yellow or light gray in gray scale) grids. Left: moving to fixed grid interpolation; right: fixed to moving grid interpolation. The nodes at the boundary of each grid receive the data from the other grid (black circle). From [5].
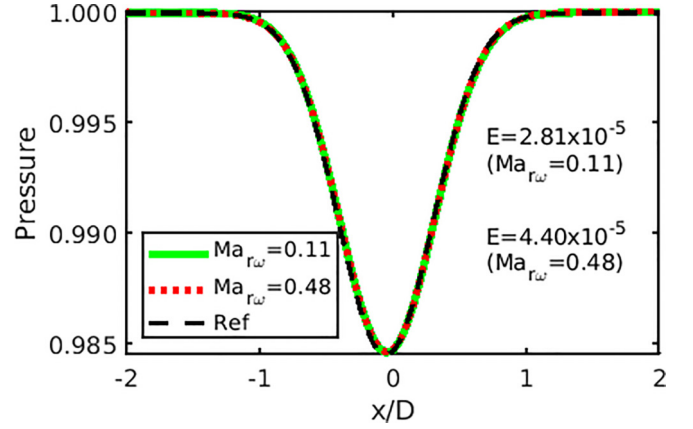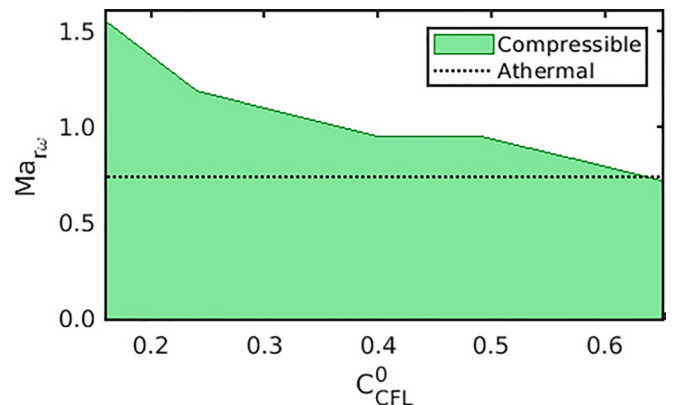

FIG. 6. Stability map of the mesh rotation speed at different CFL values.
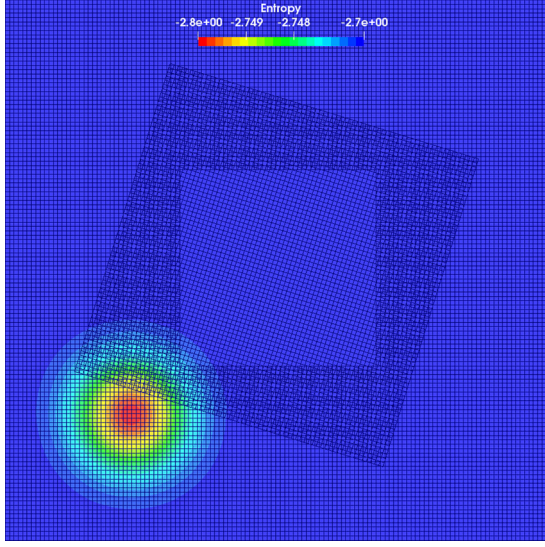
FIG. 7. Entropy spot flows over empty rotating overset grids.

FIG. 8. L2 error on the entropy for different mesh sizes. $MUSCL - 1D - \phi_n$: the MUSCL-Hancock scheme without diagonal term and a flux calculated at the current time step. $MUSCL - 2D - \phi_{n+1/2}$: the MUSCL-Hancock scheme with diagonal term and a flux calculated after half a time step.

B. Entropy spot advection

The advection of an entropy spot is then chosen to analyze the MUSCL-Hancock scheme on the rotating overset grids. The Gaussian-shaped entropy spot is initially located at the bottom left corner of the domain and is advected in time in the diagonal direction towards the top right corner (Fig. 7).

The entropy spot is initialized as

$$
\rho = \rho_0 \left[1 + \epsilon \exp \left(-\frac{(x - x_0)^2 + (y - y_0)^2}{R^2} \right) \right],
$$
$$
T = T_0 \left[1 - \epsilon \exp \left(-\frac{(x - x_0)^2 + (y - y_0)^2}{R^2} \right) \right]. \quad (20)
$$

The amplitude of the spot ϵ is set to 10^{-3} as in Farag *et al.* [1]. The advection velocities expressed as Mach numbers are $Ma_x = 0.1$ and $Ma_y = 0.1$. The number of nodes in the length of domain is varied as $N_x = [125, 160, 200, 250]$, which corresponds to the following numbers of nodes in the radius of entropy spot: $N_r = R/\Delta x = [12.5, 16, 20, 25]$. Accordingly, the number of nodes in the length of rotating domain is $N_{xr} = [100, 128, 160, 200]$. The rotation speed of the overset mesh is $Ma_{r\omega} = r\omega/c = [0.20, 0.76]$, where r is the distance between the corner of rotating mesh and the rotating center. The dynamic viscosity is negligible, fixed to $\mu = 10^{-10}$, and r_{gas} is set to 1.0. The CFL number is set as $C_{CFL}^0 = 0.2$ in terms of the advection velocity $\sqrt{Ma_x^2 + Ma_y^2}$.

The error coming from the rotating overset scheme is analyzed by comparing the entropy spot simulation using rotating overset grids and the same simulation using the same physical setup on a single fixed grid. Figure 8 shows the averaged L2 error in entropy after four flow-through times ($T_{FTT} = \sqrt{u_x^2 + u_y^2} t / \sqrt{L_x^2 + L_y^2}$), where L_x and L_y are the domain lengths in the x and y directions. The L2 error is defined as $E_S = \sqrt{\frac{\sum (s - s_{ref})^2}{N}}$, where s is the entropy value s_{ref} is the reference entropy value and N is the number of points. The two different MUSCL-Hancock schemes mentioned in Sec. II C

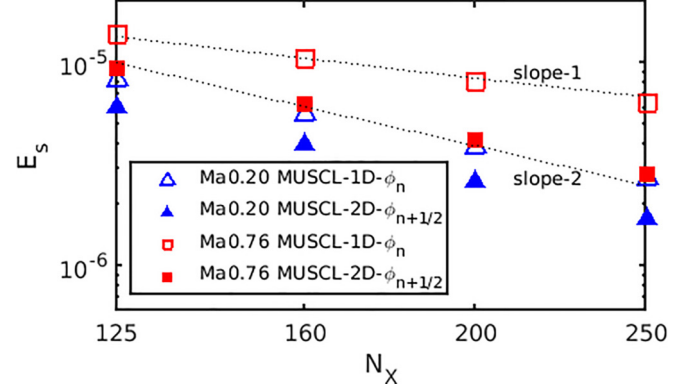are tested to study their effect on solving the entropy equation with the overset rotating grids.

Figure 8 shows that the errors are reduced by the $MUSCL - 2D - \phi_{n+1/2}$ compared to the $MUSCL - 1D - \phi_n$. Moreover, as the rotation speed is increased, the $MUSCL - 1D - \phi_n$ scheme goes down to the first-order accuracy, but $MUSCL - 2D - \phi_{n+1/2}$ remains close to the second-order accuracy. It indicates that considering the diagonal flow and unsteadiness in the MUSCL-Hancock scheme may play more significant role as its rotating speed becomes larger in the rotating overset grids.

C. Acoustic pulse

The case of an acoustic pulse is then studied to validate the rotating overset scheme with different polynomial interpolations such as the linear, quadratic, and cubic interpolations. Since the conventional athermal LBM is weakly compressible, previous references adopted a low-order linear interpolation for pressure, which was sufficient to deal with moderate pressure gradients [5,39]. However, large pressure gradients can be encountered in compressible flows, hence higher-order interpolations on pressure terms are necessary, in particular the gradient-based quadratic interpolation [5,35]. Its usage for the pressure term is described in Appendix B. A Gaussian-shaped pulse is initially located in the middle of the domain and is propagated in time through the field (Fig. 9).

The pulse is initialized as

$$
p = \left\{ \rho_0 \left[1 + \epsilon \exp \left(-\frac{(x - x_0)^2 + (y - y_0)^2}{R^2} \right) \right] \right\}^{\gamma}. \quad (21)
$$

The initial ambient density is $\rho_0 = 1$, which gives a far-field pressure close to $p_0 = 1$. The amplitude of the pulse is set to $\epsilon = 0.1$; hence a peak value of the pulse at the center is $p_{max} = 1.1$. The Gaussian pulse is discretized with $R = 10\Delta x$. The dynamic viscosity is negligible, fixed to $\mu = 10^{-10}$. The rotation speed of the overset mesh is set to $Ma_{r\omega} = r\omega/c = 0.60$. Time step is $\Delta t = 8.47 \times 10^{-3}$. The number of nodes in the length of entire domain is $Nx = 100$ and of the rotating domain is $N_{xr} = 50$.
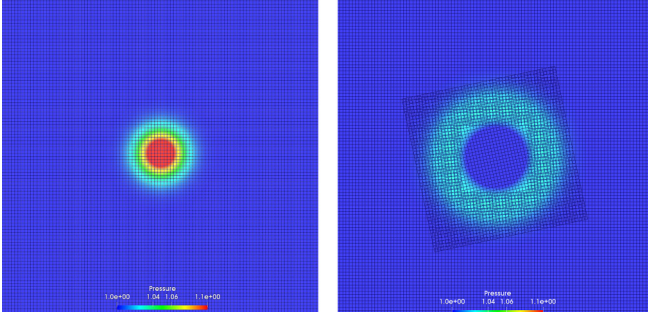
FIG. 9. Acoustic pulse propagated over the empty rotating overset grids at $t = 0$ (left) and $t = 5$ (right).

FIG. 11. Error field $|\frac{\partial p}{\partial t} - \frac{\partial p_{\text{ref}}}{\partial t}|$ of the acoustic pulse at $t = 4$: linear interpolation (left), quadratic interpolation (right).

Following the previous methodology, the error is analyzed by comparing the acoustic pulse simulation on the overset grids with regard to the same simulation on a single fixed grid. Figure 10 shows the L2-averaged error of pressure according to time. A time unit is defined by $25\Delta t$. It is reduced by increasing the interpolation order.

The same trend is observed in Fig. 11. It shows that the spurious error fields of pressure fluctuations $|\frac{\partial p}{\partial t} - \frac{\partial p_{\text{ref}}}{\partial t}|$ is reduced near the interpolation border as increasing the order from linear to quadratic.

Moreover, in this test case, it is demonstrated that there is a significant improvement between quadratic and linear interpolations, but only minor improvement from the quadratic to cubic interpolations (Fig. 10). That may be because the third-order accuracy of the quadratic interpolation is large enough not to deteriorate the second-order accuracy of the basic LBM scheme. It implies that the quadratic interpolation would be an optimal compromise to give reasonable performances in the rotating overset LBM with a low computational cost. These observations are in agreement with the theoretical study of Ref. [36] regarding the effect of the quadratic interpolations in LBM.

D. Shock-vortex interaction

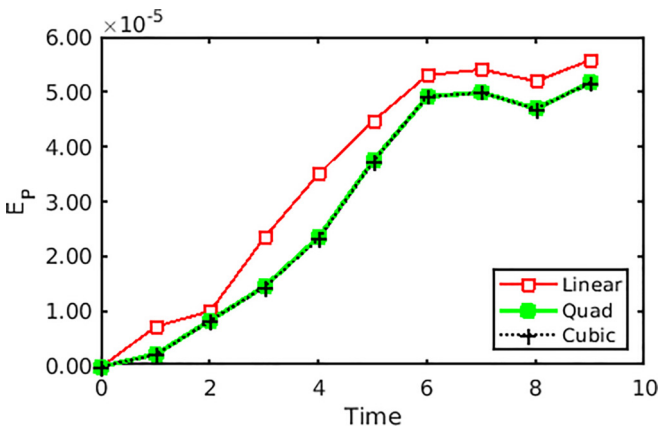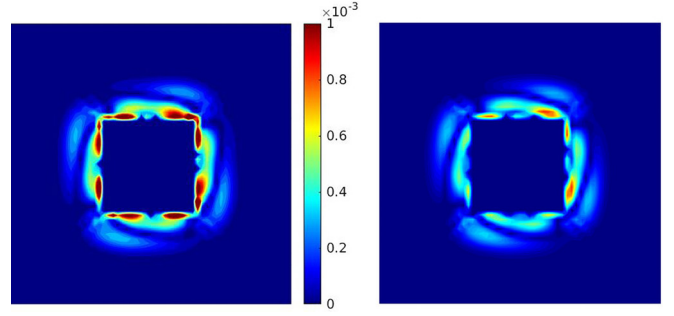The shock-vortex interaction of Inoue and Hattori [40] is now investigated in the presence of rotating overset grids. A vortex passing across a shock wave is simulated over an empty rotating overset grids. The aim is to study the stability of the shock structure over the rotating overset grids (Fig. 12).

The shock surface is initialized by [40]

$$\frac{\rho_R}{\rho_L} = \frac{u_L}{u_R} = \frac{(\gamma + 1)\text{Ma}_0^2}{(\gamma - 1)\text{Ma}_0^2 + 2},$$

$$\frac{p_R}{p_L} = 1 + \frac{2\gamma}{\gamma + 1}(\text{Ma}_0^2 - 1). \quad (22)$$

The vortex is initialized on the upstream supersonic region [Fig. 12 (left)] by

$$u_x = u_L - \sqrt{\gamma}\text{Ma}_{mv} y_c \exp\left[\frac{1}{2}[1 - (x_c^2 + y_c^2)]\right],$$

$$u_y = \sqrt{\gamma}\text{Ma}_{mv} x_c \exp\left[\frac{1}{2}[1 - (x_c^2 + y_c^2)]\right], \quad (23)$$

$$\rho_L = \left[1 - \frac{(\gamma - 1)\text{Ma}_{mv}^2}{2} \exp\left[1 - (x_c^2 + y_c^2)\right]\right]^{1/(\gamma-1)},$$

$$p_L = \rho_L^\gamma,$$

where $x_c = x - x_0$ and $y_c = y - y_0$.

Two different simulation conditions are chosen. One corresponds to a Mach number at upstream as $\text{Ma}_0 = 1.2$ and a vortex velocity is $\text{Ma}_{mv} = 0.25$, which corresponds to the test case "C" in Ref. [40]. The second one has an upstream

FIG. 10. L2-averaged error in pressure as a function of time using different polynomial interpolations.
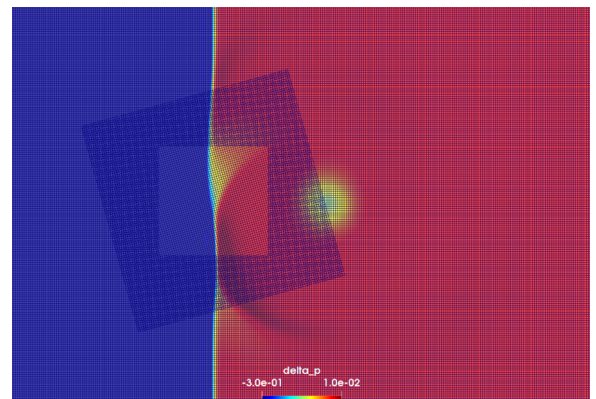

FIG. 12. A vortex passing through the shock wave simulated over the rotating overset grids.
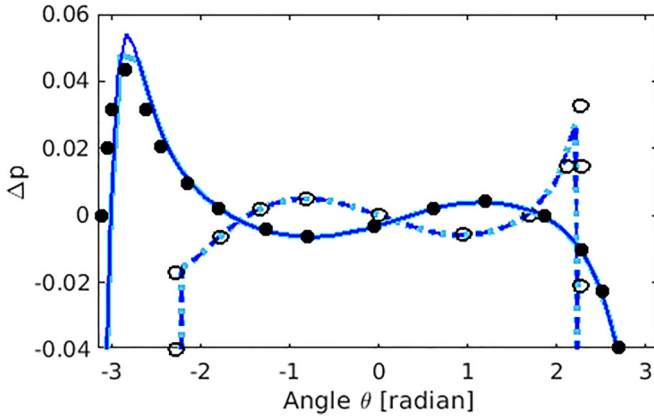
FIG. 13. Radial pressure profile Δp at $t = 6$ (case "C" in Inoue and Hattori [40]). Blue (black in gray scale) dashed line: overset LBM at $r = 6.0$. Light blue (gray in gray scale) dashed line: LBM from single mesh at $r = 6.0$. Circular marker: Inoue and Hattori at $r = 6.0$. Blue (black in gray scale) solid line: overset LBM at $r = 3.7$. Light blue (gray in gray scale) solid line: LBM from single mesh at $r = 3.7$. filled circular marker: Inoue and Hattori at $r = 3.7$.

Mach number as $Ma_0 = 1.29$ and the vortex velocity is set as $Ma_{mv} = 0.39$, which corresponds to the test case "G" in Ref. [40]. The vortex velocity Ma_{mv} indicates the local velocity at its perimeter, which is superposed to the Mach number of the advecting flow. The radius of the vortex is $R = 1$, discretized with 40 mesh points. The total number of nodes in the channel is $[1120 \times 960]$. The Reynolds number is set as $= \frac{\rho_L c R}{\mu} = 800$, where c is the upstream sound speed, ρ_L is the upstream density, and R is the radius of vortex. The vortex is initialized by Eq. (23). The distance from the rotation center to the tip of the rotating grid is $d = 5.656$, which corresponds to 226 nodes. The rotation speed of the overset mesh is $Ma_{d\omega} = d\omega/c = 0.239$. The HRR parameter is chosen as $\sigma = 1$. A Jameson shock sensor is applied to reduce numerical oscillation near the shock. More details about using the sensor in compressible LBM are given in Refs. [1,2]. The shock sensor coefficient is set as $s_c = 0.1$, and r_{gas} is set as a unity. The CFL number is set as $C_{CFL}^0 = 0.22$ in terms of the upstream advection velocity.

The shock-vortex interaction is assessed using two different references, the original reference from Inoue *et al.* [40] (cases "C" and "G") and the pressure-based HRR on a single fixed grid, which was validated by Farag *et al.* [1]. Figure 13 displays the radial profile of the normalized pressure at $t = 6R/c$, for case "C"; with $Ma_0 = 1.2$ and $Ma_{mv} = 0.25$. The normalized pressure Δp is defined as $\Delta p = (p - p_R)/p_R$ where p_R is the downstream pressure. The angle θ_{rad}, used to investigate the azimuthal pressure distribution around the vortex, follows the same definition as in Ref. [40]. In this figure, the pressure profile is plotted along the radius r from the vortex center. For $r = 6$, the pressure profile is well matched with the reference except for the shock surface near the angle $\theta_{rad} = 2.26$. However, this discrepancy is observed even without the overset mesh [1]. Therefore, this defect may due to the compressible LBM model itself rather than the overset grid scheme. For $r = 3.7$, the pressure profile of the overset scheme is in agreement with the reference except for the shock
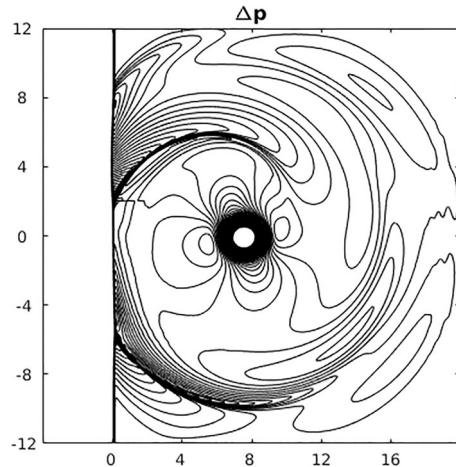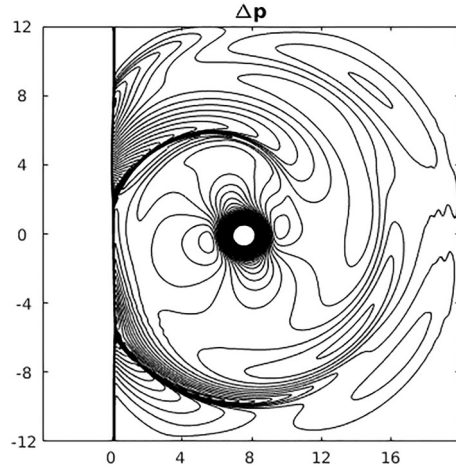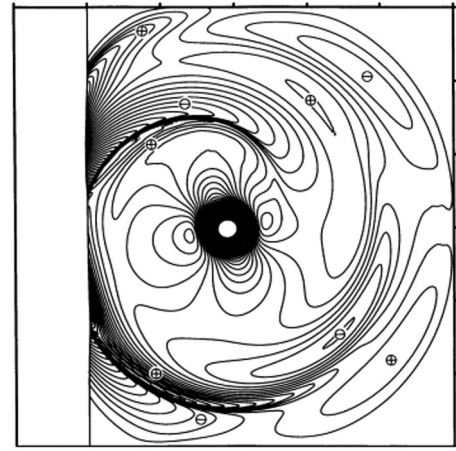

FIG. 14. Isocontours of Δp at $t = 10.3$ (case "G" in Inoue and Hattori [40]). Left: Inoue and Hattori [40]; middle: compressible LBM with a single fixed grid; right: compressible LBM with overset grids. Contour levels are the same as in Ref. [40] with $\Delta p_{min} = -0.16$, $\Delta p_{max} = 0.24$, and an increment of 0.0033.

surface near the angle $\theta_{rad} = -2.85$. Here the discrepancy of the overset scheme is larger than that of the fixed grid using the compressible LBM [1], which indicates that the numerical error originates from overset scheme.

Figure 14 compares isocontours of Δp for the case "G" in Ref. [40]. The contours are compared with those of Inoue and
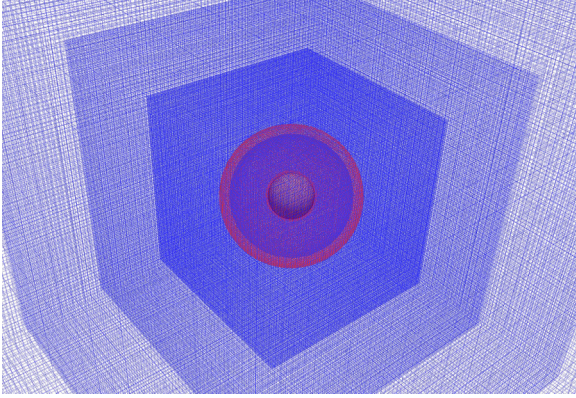
FIG. 15. Overset mesh structure for a 3D rotating sphere. Fixed mesh: blue; rotating mesh: red.

Hattori [40] and the pressure-based HRR with a single fixed grid. The figure shows that all three contours overall match well, which suggests that the overset LBM scheme can be used to simulate shock waves in rotating regions. However, a defect of the overset scheme is still observed by a nonphysical distortion in the coordinates (2,2) in the figure. Further studies are needed to improve this discrepancy, which may lead to a better capture of the shock over rotating geometries.

E. 3D rotating sphere

A 3D rotating sphere in a uniform channel flow is studied at a high Mach number (Fig. 15). The inlet Mach number is $Ma_0 = 0.8$, which corresponds to a transonic regime. The rotation ratio $a = 0.5D\omega/U_0$ is the nondimensional number, which represents the rotating speed of sphere, where D is the diameter of sphere, ω is angular velocity, and U_0 is the inflow velocity. The ratio a is varied as [0,0.6], which gives a maximum local Mach number near the surface to be $Ma = Ma_0 + aU_0/c = [0.8, 1.28]$. The Reynolds number is $Re = \frac{\rho U_0 D}{\mu} = 300$. The initial ambient pressure and density are $p_0 = 101325$ and $\rho_0 = 1.2$. There are six levels of mesh refinement, where the finest mesh has a size $\Delta x = D/64$. Each mesh refinement level has a 3D cubic shape whose specifications are described in Table II and Fig. 16. The minimum time step at the finest mesh region is set as $\Delta t = 2.076 \times 10^{-6}$.

TABLE II. Mesh refinements of the rotating sphere. D indicates the diameter of the rotating sphere. Fixed regions have a cubic shape. Rotating regions have a spherical shape. A spherical hole cutting is done in the innermost fixed region.

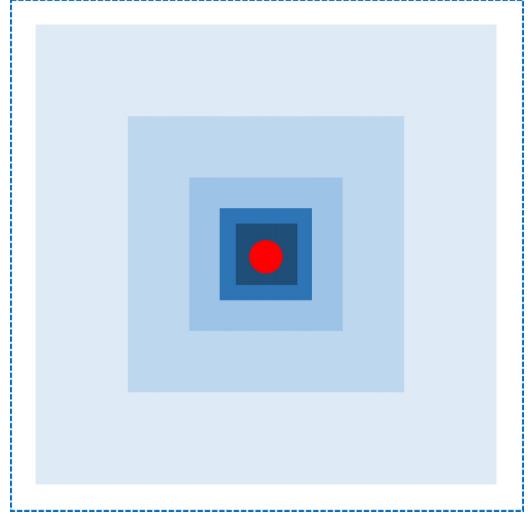| Mesh level	Length	Δx
Rotating-6 (red)	3D (diameter)	D/64
Fixed-hole cut	2.5D (diameter)	–
Fixed-6 (blue)	4D	D/64
Fixed-5 (blue)	6D	D/32
Fixed-4 (blue)	10D	D/16
Fixed-3 (blue)	18D	D/8
Fixed-2 (blue)	30D	D/4
Fixed-1 (white)	100D	D/2

FIG. 16. Mesh refinements of the rotating sphere. Fixed region: blue or gray in gray scale; rotating region: red or black in gray scale. Specifications are given in Table II.

Furthermore, the overset rotating mesh has the shape of a sphere of diameter $D_{mesh} = 3D$. The rotating sphere is located in the middle of the domain so that the distances from each boundary (inlet, outlet, and surrounding walls) are $H = 50D$. The inflow is uniform, and the surrounding boundary walls are frictionless walls. Characteristic boundary conditions are imposed to reduce the reflection from the inlet, outlet, and walls as absorbing layers [2,41]. No-slip boundary conditions are imposed on the rotating sphere with respect to the rotation reference axis, which then actualizes the rotating motion of the sphere. An adiabatic condition ($\frac{\partial T}{\partial n} = 0$) is applied on the rotating sphere surface. More details about the boundary conditions and absorbing layers are described in Refs. [2,41].

Aerodynamic coefficients are studied to validate the rotating sphere in transonic and supersonic flow regimes (Fig. 17). The coefficients are compared with the reference using high-order finite volume WENO schemes solving the Navier-Stokes equation [42]. Another reference is considered, based on the empirical regression of various simulations and experiments [43]. Averaged coefficients are computed based on the far-field integral method, following [44,45]. The aerodynamic coefficients are defined as $C_L = F_y/(0.5\rho_0 U_0^2 A)$ and $C_D = F_x/(0.5\rho_0 U_0^2 A)$, where A is the cross-sectional area of the sphere and F_x and F_y are, respectively, the horizontal and vertical integrated efforts on the surface of the sphere.

In Fig. 17 (top), the lift coefficients C_L show a correct trend, with an increase proportional to the rotation ratio. In Fig. 17 (middle) the drag coefficients C_D have larger error as the rotation ratio increases. Yet the error is still less than 10% even for the largest rotation ratio with $a = 0.6$, where the maximum local speed on the sphere surface becomes supersonic as $Ma = Ma_0 + aMa_0 = 1.26$. In Fig. 17 (bottom), the Strouhal number $St = fD/U_0$ is measured based on the frequency f of the trailing vortex behind the sphere. It shows a good trend according to the rotational ratio. All coefficients have a good tendency, which well match Ref. [42], except for the stationary case $a = 0$. In this case, flow physics are governed by the vortex shedding rather than the rotating motion of sphere, so
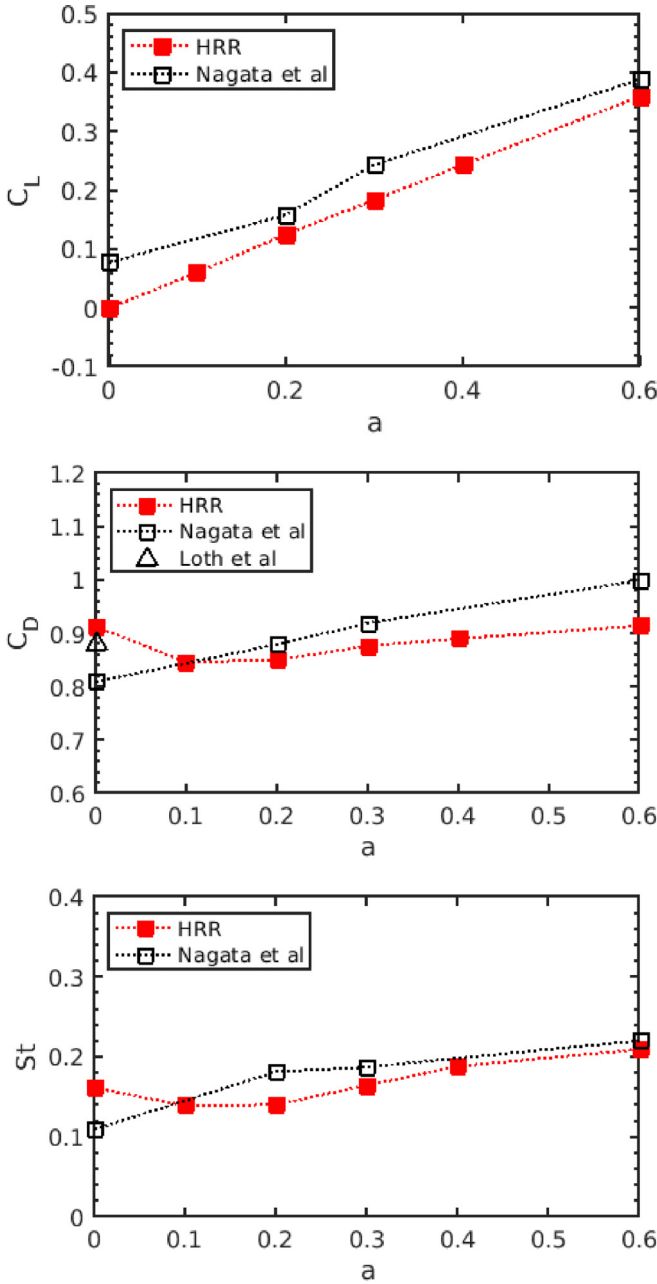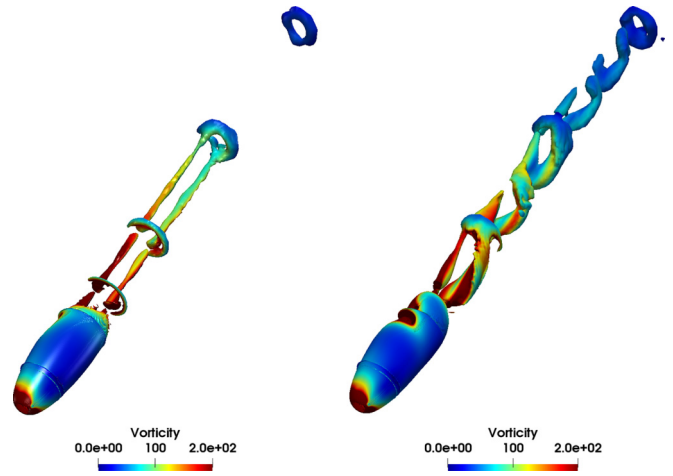
FIG. 18. Isosurface Q criterion of the rotating sphere colored by vorticity magnitude at $\mathrm{Ma}_0 = 0.8$ and $a = 0.3$. Left: $\mathrm{MUSCL} - 1D - \phi_n$ scheme; right: $\mathrm{MUSCL} - 2D - \phi_{n+1/2}$ scheme.

the finest mesh region is extended to capture more clearly the trailing vortex structures. It clearly demonstrates that the higher-order MUSCL scheme ($\mathrm{MUSCL} - 2D - \phi_{n+1/2}$) successfully captures the downstream rotating vortex structure. On the contrary, the low-order MUSCL-Hancock scheme ($\mathrm{MUSCL} - 1D - \phi_n$) is not able to do so, which implies that the higher-order MUSCL-Hancock scheme is more appropriate to recover the unsteady vortex structure due to its lower numerical dissipation.

F. Caradonna and Tung rotor

The Caradonna and Tung rotor [46] is tested to validate the overset rotating scheme for industrial applications in high Mach compressible flow regimes. This is a two-bladed rotor, composed of NACA0012 profiles. Its aspect ratio is $\mathrm{AR} = R/l = 6$, where R is the radius of the rotor and l is the chord length. The Mach number at the tip of rotor is $\mathrm{Ma}_{tip} = 0.723$. The Reynolds number is $\mathrm{Re} = \frac{\rho_0 U_{tip} l}{\mu} = 3.2 \times 10^6$, where ρ_0 is the ambient density. The initial ambient density is set to $\rho_0 = 1.2$, and the initial ambient pressure is $p_0 = 101325$. The collective pitch angle (or angle of attack in this test case) is $\theta_c = 2°$.

A large eddy simulation (LES) model, more precisely the Vreman subgrid turbulence model, is applied to consider turbulent flows [47]. An explicit wall model is used to take into account the turbulent boundary layer near the rotating solid walls [48]. The Vreman LES model and explicit wall model have been chosen since they are validated with the pressure-based HRR-LBM in the context of high Mach turbulent flows [2].

The finest mesh close to the rotating walls is $\Delta x = l/200$, which leads to $y+ \approx 110$ at the tip of the rotor ($r/R = 0.96$) and $y^+ \approx 90$ in the middle of the blade span ($r/R = 0.5$); $y+$ is estimated as $y+ = \frac{u_\tau \Delta x}{\nu}$. Seven different mesh refinement levels are considered, as illustrated in Figs. 19, 20 and Table III. The minimum time step at the finest mesh region is set as $\Delta t = 2.889 \times 10^{-6}$.

FIG. 17. Aerodynamic coefficients of a 3D rotating sphere at $\mathrm{Ma}_0 = 0.8$. Maximum local Mach number on the sphere is $\mathrm{Ma}_{lcl} = \mathrm{Ma}_0 + a \times \mathrm{Ma}_0$.

that it may highly depend on the mesh resolution or the mesh refinement structure. The finest mesh size considered in the compressible LBM simulation is $\Delta x = D/64$, while Nagata et al. [42] adopted a finer mesh with $\Delta x = D/306.5$. Moreover, Nagata et al. [42] extended the mesh in the wake region to capture details of wake physics. Therefore, Ref. [43] is also considered to support the results at the stationary condition [Fig. 17 (bottom)].

Vortex structures are visualized in Fig. 18, where isosurfaces of the Q criterion are colored with the vorticity magnitude, to highlight the effect of the different MUSCL-Hancock schemes ($\mathrm{MUSCL} - 1D - \phi_n$ and $\mathrm{MUSCL} - 2D - \phi_{n+1/2}$ described in Sec. IIC). The stream-wise length of

TABLE III. Mesh refinement levels of the Caradonna and Tung rotor. l indicates the chord length of the rotor (Fig. 20, left). The outer boundary has a cubic shape (referred to as "fixed-1" in the table). All fixed regions have a circular cylindrical shape. Refinement levels in the rotating region have both cylinder and rectangular shapes. A cylindrical hole cutting is done in the innermost fixed region.

Mesh level	Height	Radius	Δx
Rotating-7 (red)	$0.25l$	$1.55l$ (length)	$l/200$
Rotating-6 (red)	$0.45l$	$1.85l$ (length)	$l/100$
Rotating-5 (red)	$2.0l$	$7l$	$l/50$
Fixed-hole cut	$1.2l$	$6.7l$	–
Fixed-5 (blue)	$3.75l$	$7.25l$	$l/50$
Fixed-4 (blue)	$5.0l$	$7.75l$	$l/25$
Fixed-3 (blue)	$7.5l$	$8.75l$	$l/12.5$
Fixed-2 (blue)	$11.25l$	$10l$	$l/6.25$
Fixed-1 (white)	$40l$	$40l$ (length)	$l/3.125$

Figure 24 provides a visualization of the vortex structure, using isosurfaces of the Q criterion colored by the vorticity magnitude. It exhibits turbulent fluctuations on the rotor surface and a trailing vortex behind the rotor. Figure 25 demonstrates the effect of the higher-order MUSCL-Hancock scheme (MUSCL $- 2D - \phi_{n+1/2}$). Spurious noise around the vortex ring is reduced by using the higher-order MUSCL-Hancock scheme. This implies that the higher-order scheme
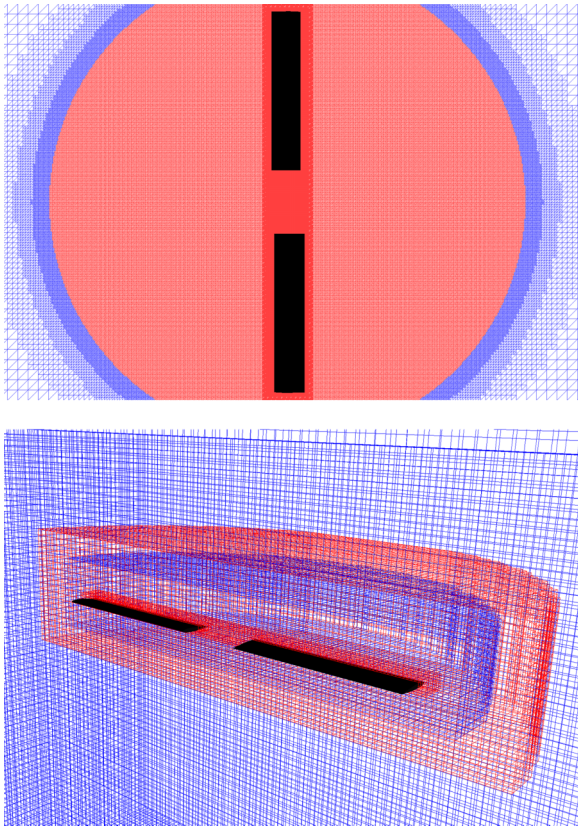
FIG. 19. The rotating overset grids structure for the Caradonna and Tung rotor [46]. Fixed mesh (blue), rotating mesh (red), and the rotor (black). Top: top view; bottom: isometric view.

The computational domain has a cubic shape, and the far-field boundaries are located at $H = \frac{20}{l}$ from the center of rotor. Characteristic pressure boundary conditions are applied at these boundaries to reduce spurious acoustic reflections [2,41].

Figures 21–23 compare pressure coefficients with the reference experiments [46]. They are defined as $C_p = (p - p_0/[0.5\rho_0(\omega r)^2]$, where p_0 is the ambient pressure and ω is the angular velocity of the rotor. The pressure coefficients are compared to the reference at different spanwise locations ($r/R = 0.5, 0.8, 0.96$), and a correct agreement can be noticed.
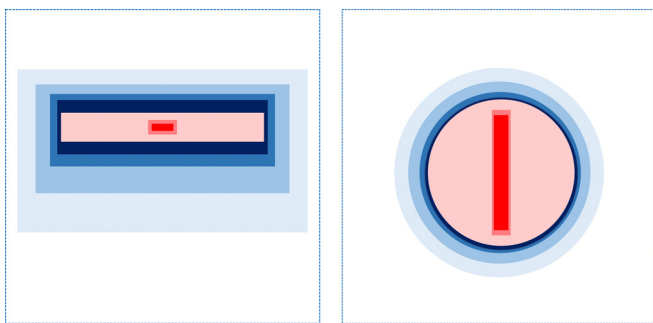

FIG. 20. Mesh refinement structure of the Caradonna and Tung rotor. Left: side view; right: top view. Specifications are given in Table III.
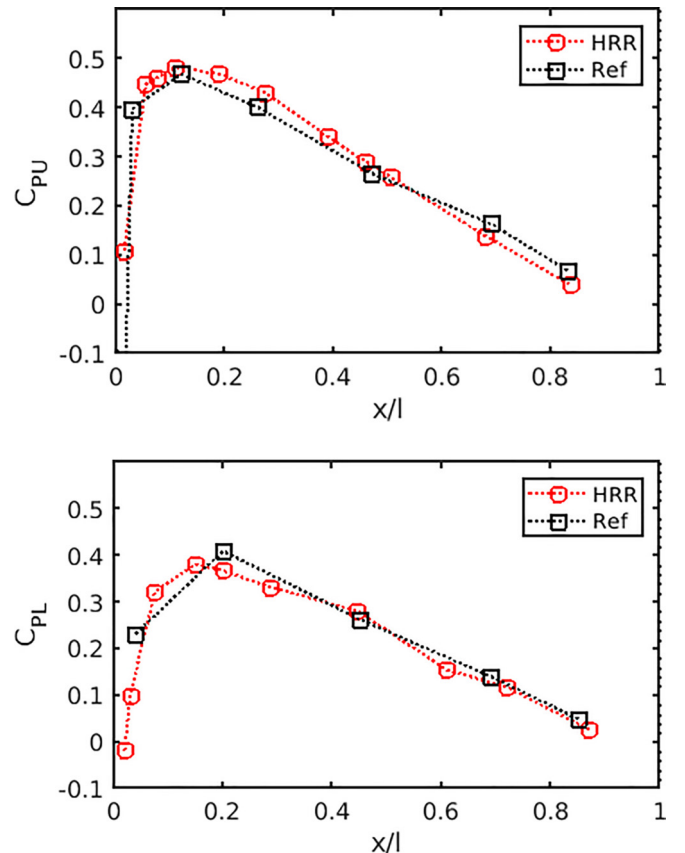

FIG. 21. Pressure coefficients at $r/R = 0.5$ cross section. Top: upper surface; bottom: lower surface.

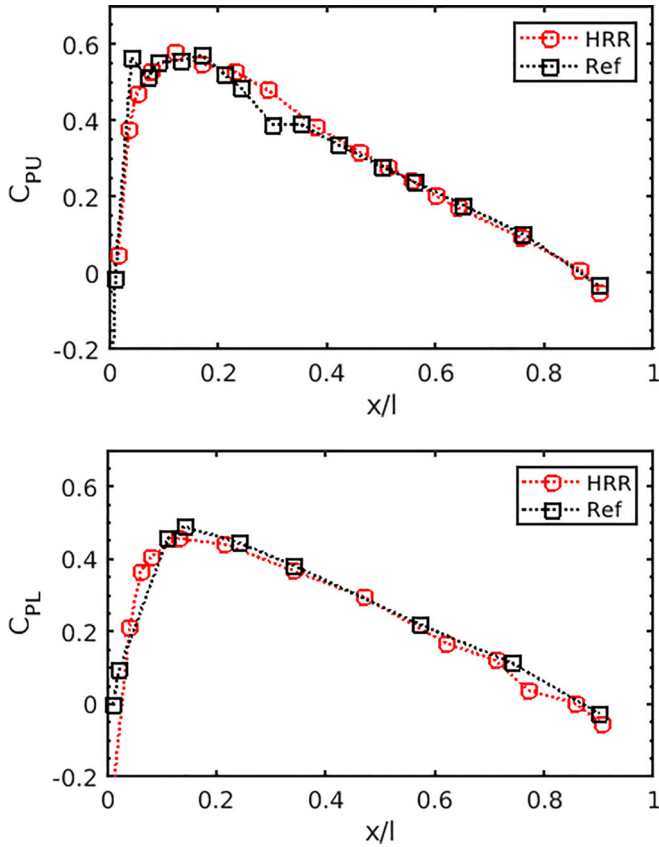FIG. 22. Pressure coefficients at $r/R = 0.8$ cross section. Top: upper surface; bottom: lower surface.

FIG. 23. Pressure coefficients at $r/R = 0.96$ cross section. Top: upper surface; bottom: lower surface.

would be more appropriate when acoustic properties need to be accurately captured.

IV. CONCLUSION

This work validates the rotating overset grids coupled with the compressible LBM for high Mach compressible flows. The objective is first to demonstrate that this compressible LBM with the overset grids is of second-order accuracy, as for the classic LBM. This is done by controlling the error level of the compressible overset schemes coming from different sources to be less than or at least equal to the second order, so that the errors do not spoil the baseline accuracy of LBM. Subsequently, the rotating scheme shows its robustness by being tested for high Mach configurations such as the rotating sphere, and a 3D rotor with the wall-modeled LES.

First, Sec. II A suggests how to apply the compressible LBM in a noninertial rotating reference frame. The fictitious forces are properly considered in collision and streaming steps of the compressible LBM. This leads to an increase of the maximum rotation velocity of the overset rotating grid (see Secs. III A and III D).

Next, we investigate how the fixed inertial mesh and rotating noninertial mesh communicate to each other through a polynomial interpolation, yielding an inevitable numerical error. This work applies the gradient-based quadratic interpolation having a $O(\Delta x^3)$ numerical error. We employ this

interpolation not only for velocities, but also for the pressure related variables (ρ, θ) so that it can take into account the large pressure gradient of compressible flow. Also, it is found that the quadratic interpolation has the optimal order of accuracy and computational cost compared to higher-order
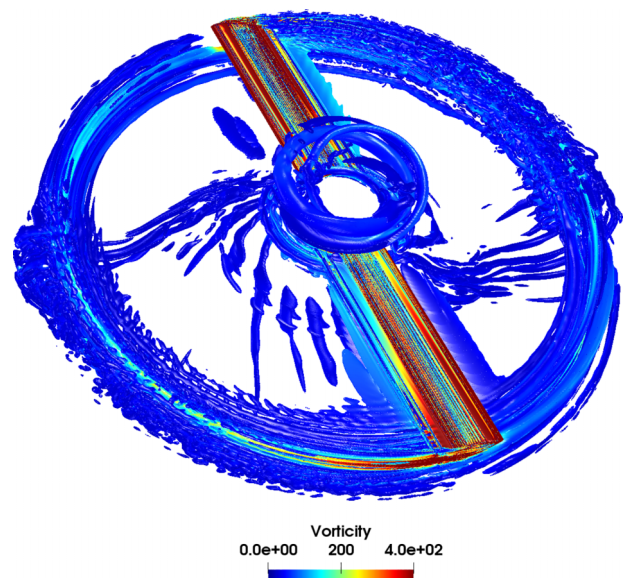
FIG. 24. Isometric view of the isosurface Q criterion colored by vorticity magnitude from the higher-order MUSCL-Hancock scheme (MUSCL $- 2D - \phi_{n+1/2}$).

FIG. 25. Top view of the cross-sectional surface colored by vorticity magnitude. Left: $MUSCL - 1D - \phi_n$; right: $MUSCL - 2D - \phi_{n+1/2}$.

interpolation such as the cubic interpolation (see Secs. II D and III C).

Moreover, the higher-order MUSCL-Hancock scheme, which transports temperature in compressible flow, is designed to reduce the coupling error with LBM in rotating grids. In this work, exploiting the fact that the rotating region has multidire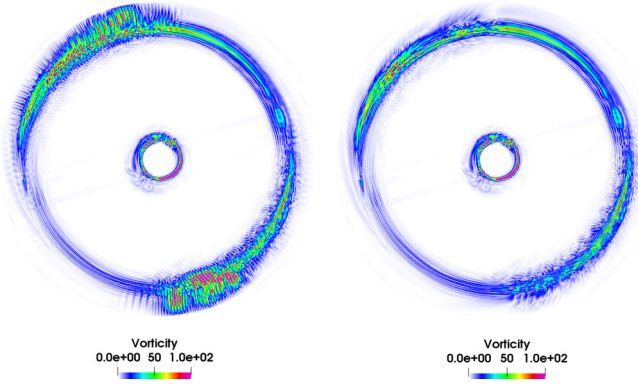ctional fluxes and the scheme is coupled with the LBM via velocity, the numerical error can be reduced by both considering the diagonal fluxes in the MUSCL-Hancock scheme and taking the velocity after the half time step from the LBM. Thus, it proposes a third-order accuracy for constant and unidirectional flows, and a second-order accuracy even for nonconstant and multidirectional flows. This contributes to securing the second-order accuracy of this scheme like the classic LBM by properly managing the coupling error between LBM and the MUSCL-Hancock scheme (Secs. II C and III B).

Then the rotating overset scheme with compressible LBM demonstrates its capability to simulate rotating solid geometries in high Mach compressible flows by being compared with experiments and conventional finite volume methods. It is validated for a rotating sphere in a laminar high Mach regime (Ma = 0.8) and the Caradonna and Tung rotor test case using wall-modeled LES at Ma = 0.723 and Re = 3×10^6 (Secs. III E and III F).

To authors' knowledge, this is the first demonstration on moving geometries for high Mach compressible flows by using LBM, among any type of motion (oscillation, rotation) and any numerical method (overset grids, ALE, IBM). The authors expect that this work can be applied to industrial applications such as rotors or turbofans. Further studies include an in-depth focus on the boundary conditions to recover more severe shocks over the rotating geometries, conservative energy schemes to better consider the flow discontinuity at the rotating grid borders, and fluid-structure interactions with compressible flows.

APPENDIX A: TAYLOR EXPANSION ON THE MUSCL-HANCOCK SCHEME

In this work the unsplit multidirectional MUSCL-Hancock scheme is suggested to take into account diagonal fluxes and unsteadiness in the rotating overset region ($MUSCL - 2D - \phi_{n+1/2}$). Its order of accuracy is detailed here using Taylor expansions. Also, as a reference, the MUSCL-Hancock scheme accounting for unidirectional fluxes and not considering unsteadiness is also studied ($MUSCL - 1D - \phi_n$). The order of accuracy is described for two different conditions. One is the 1D flow with nonconstant velocity. In this condition, it highlights the effect of calculating the fluxes using the velocity after half a time step ($\phi_{n+1/2}$). The second one is the multidirectional flow with constant velocity, where the difference made by adding the diagonal fluxes is scrutinized ($MUSCL - 2D$).

1. 1D advection equation with nonconstant velocity

We consider the 1D advection equation with nonconstant velocity,

$$\frac{\partial s}{\partial t} + u(x,t)\frac{\partial s}{\partial x} = 0. \tag{A1}$$

The MUSCL-Hancock scheme using the velocity after half a time step $u(x, t + \Delta t/2)$ which aims at solving this equation reads ($MUSCL - \phi_{n+1/2}$)

$$s(x, t + \Delta t) = s(x,t) + u(x, t + \Delta t/2)$$
$$\times \frac{\Delta t}{\Delta x}[F_{+1/2}(x - \Delta x, t) - F_{+1/2}(x,t)], \tag{A2}$$

where $F_{+1/2}$ is the right intercell flux. When $u(x,t) \geqslant 0$, it is defined as

$$F_{+1/2}(x,t) = s_R(x,t) + \frac{\Delta t}{\Delta x}\frac{u(x,t)}{2}[s_L(x,t) - s_R(x,t)], \tag{A3}$$

where

$$s_R(x,t) = s(x,t) + \frac{\Delta(x,t)}{2}, \tag{A4}$$

$$s_L(x,t) = s(x,t) - \frac{\Delta(x,t)}{2}, \tag{A5}$$

and

$$\Delta(x,t) = \frac{1}{2}\{(1 + \eta)[s(x,t) - s(x - \Delta x, t)]$$
$$+ (1 - \eta)[s(x + \Delta x, t) - s(x,t)]\}, \tag{A6}$$

with

$$\eta = \frac{1}{3}\left(2\frac{\Delta t}{\Delta x}u(x,t) - \text{sgn}[u(x,t)]\right). \tag{A7}$$

Here we consider the case $u(x, t) \geqslant 0$. By expanding the defined MUSCL-Hancock scheme on space, one has

$$s_L(x, t) - s_R(x, t) = -\Delta x \frac{\partial s}{\partial x} + \eta(x, t) \frac{\Delta x^2}{2} \frac{\partial^2 s}{\partial x^2} + O(\Delta x^3). \tag{A8}$$

Then

$$F_{+1/2}(x, t) = s(x, t) + \left(1 - u\frac{\Delta t}{\Delta x}\right)$$
$$\times \left(\frac{\Delta x}{2}\frac{\partial s}{\partial x} - \eta(x, t)\frac{\Delta x^2}{4}\frac{\partial^2 s}{\partial x^2}\right) + O(\Delta x^3), \tag{A9}$$

$$F_{+1/2}(x - \Delta x, t) = s(x, t) - \left(1 + u\frac{\Delta t}{\Delta x}\right)\frac{\Delta x}{2}\frac{\partial s}{\partial x}$$
$$+ \left((2 + \eta)u\frac{\Delta t}{\Delta x} - \eta\right)\frac{\Delta x^2}{4}\frac{\partial^2 s}{\partial x^2}$$
$$+ \left(2\frac{\partial u}{\partial x}\frac{\Delta t}{\Delta x}\right)\frac{\Delta x^2}{4}\frac{\partial s}{\partial x} + O(\Delta x^3). \tag{A10}$$

This gives

$$F_{+1/2}(x - \Delta x, t) - F_{+1/2}(x, t)$$
$$= -\Delta x \frac{\partial s}{\partial x} + u\frac{\Delta t}{\Delta x}\frac{\Delta x^2}{2}\frac{\partial^2 s}{\partial x^2}$$
$$+ \left(2\frac{\partial u}{\partial x}\frac{\Delta t}{\Delta x} - \frac{\partial^2 u}{\partial x^2}\Delta t\right)\frac{\Delta x^2}{4}\frac{\partial s}{\partial x} + O(\Delta x^3). \tag{A11}$$

The Taylor expansion on the MUSCL scheme (A2) yields the entropy equation and subsidiary high-order error terms as

$$\frac{\partial s}{\partial t} + u\frac{\partial s}{\partial x} = -\frac{\Delta t}{2}\frac{\partial^2 s}{\partial t^2} + u^2\frac{\Delta t}{2}\frac{\partial^2 s}{\partial x^2} + u\left(2\frac{\partial u}{\partial x}\frac{\Delta t}{\Delta x}\right)\frac{\Delta x}{4}\frac{\partial s}{\partial x}$$
$$+ \frac{1}{2}\frac{\partial u}{\partial t}\left(-\Delta t\frac{\partial s}{\partial x}\right) + O(\Delta t^2). \tag{A12}$$

Let us derivate this expression by time. It yields

$$\frac{\partial^2 s}{\partial t^2} + u\frac{\partial^2 s}{\partial x \partial t} + \frac{\partial u}{\partial t}\frac{\partial s}{\partial x} = O(\Delta t). \tag{A13}$$

The expression of $\partial^2 s / \partial x \partial t$ can be obtained by deriving Eq. (A12) by space:

$$\frac{\partial^2 s}{\partial x \partial t} + u\frac{\partial^2 s}{\partial x^2} + \frac{\partial u}{\partial x}\frac{\partial s}{\partial x} = O(\Delta t). \tag{A14}$$

One then obtains

$$\frac{\partial^2 s}{\partial t^2} = u^2\frac{\partial^2 s}{\partial x^2} + u\frac{\partial u}{\partial x}\frac{\partial s}{\partial x} - \frac{\partial u}{\partial t}\frac{\partial s}{\partial x} + O(\Delta t). \tag{A15}$$

Injecting it in Eq. (A12) yields

$$\frac{\partial s}{\partial t} + u\frac{\partial s}{\partial x} = O(\Delta t^2). \tag{}$$

Therefore, the MUSCL $- \phi_{n+1/2}$ scheme is second-order accurate for 1D nonconstant flow.

Now let us derive the accuracy of MUSCL $- \phi_n$, which adopts velocity at the current time step as in Eq. (A2):

$$s(x, t + \Delta t) = s(x, t) + u(x, t)\frac{\Delta t}{\Delta x}$$
$$\times [F_{+1/2}(x - \Delta x, t) - F_{+1/2}(x, t)]. \tag{A16}$$

The Taylor expansion on this MUSCL-Hancock scheme yields

$$\frac{\partial s}{\partial t} + u\frac{\partial s}{\partial x} = -\frac{\Delta t}{2}\frac{\partial^2 s}{\partial t^2} + u^2\frac{\Delta t}{2}\frac{\partial^2 s}{\partial x^2} + u\left(2\frac{\partial u}{\partial x}\frac{\Delta t}{\Delta x}\right)\frac{\Delta x}{4}\frac{\partial s}{\partial x}$$
$$+ O(\Delta t^2). \tag{A17}$$

Arranging it using the expression (A15) gives

$$\frac{\partial s}{\partial t} + u\frac{\partial s}{\partial x} = O(\Delta t). \tag{A18}$$

Therefore, the MUSCL $- \phi_n$ scheme is first order accurate for 1D nonconstant flow.

2. Multidirectional advection equation with constant velocity

The multidimensional entropy equation is

$$\frac{\partial s}{\partial t} + \sum_{\alpha \in \{x,y,z\}} u_\alpha \frac{\partial s}{\partial \alpha} = 0, \tag{A19}$$

where an implicit summation is done on $\alpha \in \{x, y, z\}$.

The MUSCL-Hancock scheme which aims at solving this equation reads

$$s(\boldsymbol{x}, t + \Delta t) = s(\boldsymbol{x}, t) + \sum_{\alpha \in \{x,y,z\}} u_\alpha \frac{\Delta t}{\Delta x}$$
$$\times [F_{+\Delta\alpha/2}(\boldsymbol{x} - \boldsymbol{e_\alpha}\Delta x, t) - F_{+\Delta\alpha/2}(\boldsymbol{x}, t)], \tag{A20}$$

where $F_{+\Delta\alpha/2}$ is defined, for $u_\alpha \geqslant 0$, as

$$F_{+\Delta\alpha/2}(\boldsymbol{x}, t) = s(\boldsymbol{x}, t) + \frac{1}{2}\Delta_\alpha(\boldsymbol{x}, t) - \sum_{\beta \in \{x,y,z\}} \frac{u_\beta}{2}\frac{\Delta t}{\Delta x}\Delta_\beta(\boldsymbol{x}, t), \tag{A21}$$

where

$$\Delta_\alpha(\boldsymbol{x}, t) = \frac{1}{2}\{(1 + \eta_\alpha)[s(\boldsymbol{x}, t) - s(\boldsymbol{x} - \boldsymbol{e_\alpha}\Delta x, t)$$
$$+ (1 - \eta_\alpha)(s(\boldsymbol{x} + \boldsymbol{e_\alpha}\Delta x, t) - s(\boldsymbol{x}, t)]\} \tag{A22}$$

and

$$\eta_\alpha = \frac{1}{3}\left[2\frac{\Delta t}{\Delta x}u_\alpha - \text{sgn}(u_\alpha)\right]. \tag{A23}$$

A Taylor expansion of this slope when $u_\alpha \geqslant 0$ yields

$$\Delta_\alpha(\boldsymbol{x}, t) = \Delta x \frac{\partial s}{\partial \alpha} - \eta_\alpha \frac{\Delta x^2}{2}\frac{\partial^2 s}{\partial \alpha^2} + \frac{\Delta x^3}{6}\frac{\partial^3 s}{\partial \alpha^3} + O(\Delta x^4). \tag{A24}$$

Hence, after some math, one has

$$
F_{+\Delta\alpha/2}(\boldsymbol{x} - \boldsymbol{e_\alpha}\Delta x, t) - F_{+\Delta\alpha/2}(\boldsymbol{x}, t)
$$

$$
= -\Delta x \frac{\partial s}{\partial \alpha} + \frac{\Delta x^2}{2} u_\beta \frac{\Delta t}{\Delta x} \frac{\partial^2 s}{\partial \alpha \partial \beta}
$$

$$
+ \frac{\Delta x^3}{12} \left((1 + 3\eta_\alpha) \frac{\partial^3 s}{\partial \alpha^3} - 3u_\beta \frac{\Delta t}{\Delta x} \frac{\partial^3 s}{\partial \alpha^2 \partial \beta} \right.
$$

$$
\left. - 3u_\beta \eta_\beta \frac{\Delta t}{\Delta x} \frac{\partial^3 s}{\partial \beta^2 \partial \alpha} \right) + O(\Delta x^4). \tag{A25}
$$

The Taylor expansion of the MUSCL-Hancock scheme (A20) yields the entropy equation and subsidiary high-order error terms as

$$
\frac{\partial s}{\partial t} + u_\alpha \frac{\partial s}{\partial \alpha}
$$

$$
= \frac{\Delta t}{2} \left(-\frac{\partial^2 s}{\partial t^2} + u_\alpha u_\beta \frac{\partial^2 s}{\partial \alpha \partial \beta} \right)
$$

$$
+ \frac{\Delta t^2}{12} \left\{ -2 \frac{\partial^3 s}{\partial t^3} + u_\alpha \frac{\Delta x^2}{\Delta t^2} \left[(1 + 3\eta_\alpha) \frac{\partial^3 s}{\partial \alpha^3} \right. \right.
$$

$$
\left. \left. - 3u_\beta \frac{\Delta t}{\Delta x} \frac{\partial^3 s}{\partial \alpha^2 \partial \beta} - 3u_\beta \eta_\beta \frac{\Delta t}{\Delta x} \frac{\partial^3 s}{\partial \beta^2 \partial \alpha} \right] \right\} + O(\Delta t^3). \tag{A26}
$$

All the time derivative terms can be arranged as in the previous Appendix A 1. Finally, it leads to

$$
\frac{\partial s}{\partial t} + u_\alpha \frac{\partial s}{\partial \alpha} = \frac{\Delta t^2}{12} u_\alpha \left[2u_\beta \frac{\partial^2}{\partial \alpha \partial \beta} \left(u_\gamma \frac{\partial s}{\partial \gamma} - u_\beta \frac{\partial s}{\partial \beta} \right) \right.
$$

$$
\left. + 2u_\alpha \frac{\Delta x}{\Delta t} \frac{\partial^3 s}{\partial \alpha^3} + u_\beta \frac{\Delta x}{\Delta t} \frac{\partial^2}{\partial \alpha \partial \beta} \left(\frac{\partial s}{\partial \beta} - 3 \frac{\partial s}{\partial \alpha} \right) \right]
$$

$$
+ O(\Delta t^3). \tag{A27}
$$

In 1D constant velocity, the MUSCL $- 2D$ scheme including the diagonal fluxes reads

$$
\frac{\partial s}{\partial t} + u_x \frac{\partial s}{\partial x} = O(\Delta t^3). \tag{A28}
$$

In 2D constant velocity, it reads

$$
\frac{\partial s}{\partial t} + u_x \frac{\partial s}{\partial x} + u_y \frac{\partial s}{\partial y} = O(\Delta t^2). \tag{A29}
$$

Now, the accuracy of MUSCL-Hancock scheme without the diagonal fluxes, MUSCL $- 1D$, is investigated for a multidirectional constant velocity flow. The advection equation is written as in Eqs. (A19) and (A20). However, the flux now reads

$$
F_{+\Delta\alpha/2}(\boldsymbol{x}, t) = s(\boldsymbol{x}, t) + \frac{1}{2} \Delta_\alpha(\boldsymbol{x}, t) - \frac{u_\alpha}{2} \frac{\Delta t}{\Delta x} \Delta_\alpha(\boldsymbol{x}, t). \tag{A30}
$$

A Taylor expansion of this scheme leads to

$$
\frac{\partial s}{\partial t} + u_\alpha \frac{\partial s}{\partial \alpha} = \frac{\Delta t}{2} \left(-\frac{\partial^2 s}{\partial t^2} + u_\alpha^2 \frac{\partial^2 s}{\partial \alpha^2} \right)
$$

$$
+ \frac{\Delta t^2}{12} \left(-2 \frac{\partial^3 s}{\partial t^3} + u_\alpha \frac{\Delta x^2}{\Delta t^2} \left[(1 + 3\eta_\alpha) \frac{\partial^3 s}{\partial \alpha^3} \right. \right.
$$

$$
\left. \left. - 3u_\alpha \frac{\Delta t}{\Delta x} \frac{\partial^3 s}{\partial \alpha^3} - 3u_\alpha \eta_\alpha \frac{\Delta t}{\Delta x} \frac{\partial^3 s}{\partial \alpha^3} \right] \right) + O(\Delta t^3). \tag{A31}
$$

All the time derivative terms can be arranged as in the previous Appendix A 1. Finally, it leads to

$$
\frac{\partial s}{\partial t} + u_\alpha \frac{\partial s}{\partial \alpha} = \frac{\Delta t}{2} \left(-u_\alpha u_\beta \frac{\partial^2 s}{\partial \alpha \partial \beta} + u_\alpha^2 \frac{\partial^2 s}{\partial \alpha^2} \right)
$$

$$
+ \frac{\Delta t^2}{12} \left(-4u_\alpha u_\beta u_\gamma \frac{\partial^3 s}{\partial \alpha \partial \beta \partial \gamma} + 3u_\alpha u_\beta^2 \frac{\partial^3 s}{\partial \beta^2 \partial \alpha} \right.
$$

$$
\left. + 3u_\alpha^2 u_\beta \frac{\partial^3 s}{\partial \alpha^2 \partial \beta} - 2u_\alpha^3 \frac{\partial^3 s}{\partial \alpha^3} \right) + O(\Delta t^3). \tag{A32}
$$

For a 1D constant velocity, the MUSCL $- 1D$ scheme without the diagonal fluxes gives a third-order accuracy as

$$
\frac{\partial s}{\partial t} + u_x \frac{\partial s}{\partial x} = O(\Delta t^3). \tag{A33}
$$

For a 2D constant velocity, it is first-order accurate as

$$
\frac{\partial s}{\partial t} + u_x \frac{\partial s}{\partial x} + u_y \frac{\partial s}{\partial y} = O(\Delta t). \tag{A34}
$$

Here the first-order error term $O(\Delta t) \sim u_x u_y \frac{\partial^2 s}{\partial x \partial y}$ behaves like numerical viscosity and may lead to instability when it has a negative value [49].

APPENDIX B: THE GRADIENT-BASED QUADRATIC INTERPOLATION

The gradient-based quadratic interpolation was suggested and tested in Refs. [5,35,39]. This interpolation was proved to have the third-order accuracy $O(\Delta x^3)$ [35]. The references used the interpolation only for velocity fields, but this work expands this interpolation to macroscopic variables such as density ρ and temperature θ, and we provide here the details of this implementation.

The polynomial interpolation reads

$$
p_i(\bar{x}, \bar{y}, \bar{z}) = a_0 + a_1 \bar{x} + a_2 \bar{y} + a_3 \bar{z} + b_1 \bar{x}\bar{y} + b_2 \bar{x}\bar{z} + b_3 \bar{y}\bar{z}
$$

$$
+ c_1(1 - \bar{x}^2) + c_2(1 - \bar{y}^2) + c_3(1 - \bar{z}^2), \quad \text{(B1)}
$$

where $\bar{x} = \frac{2(x - x_0)}{h} - 1$, $\bar{y} = \frac{2(y - y_0)}{h} - 1$, $\bar{z} = \frac{2(z - z_0)}{h} - 1$, h is the length of uniform Cartesian mesh, and (x_0, y_0, z_0)

indicates the coordinates of one reference donor node:

$$
\begin{bmatrix} a_0 \\ a_1 \\ a_2 \\ a_3 \\ b_1 \\ b_2 \\ b_3 \end{bmatrix} = \frac{1}{8} \begin{bmatrix} 1 & 1 & 1 & 1 & 1 & 1 & 1 & 1 \\ -1 & 1 & 1 & -1 & -1 & 1 & 1 & -1 \\ -1 & -1 & 1 & 1 & -1 & -1 & 1 & 1 \\ -1 & -1 & -1 & -1 & 1 & 1 & 1 & 1 \\ 1 & -1 & 1 & -1 & 1 & -1 & 1 & -1 \\ 1 & -1 & -1 & 1 & -1 & 1 & 1 & -1 \\ 1 & 1 & -1 & -1 & -1 & -1 & 1 & 1 \end{bmatrix} \begin{bmatrix} p(0,0,0) \\ p(h,0,0) \\ p(h,h,0) \\ p(0,h,0) \\ p(0,0,h) \\ p(h,0,h) \\ p(h,h,h) \\ p(0,h,h) \end{bmatrix},
\tag{B2}
$$

where eight donor nodes $p(x, y, z)$ are expressed in terms of original coordinates (x, y, z), and

$$
c_1 = \frac{1}{32} \begin{bmatrix} 1 & -1 & -1 & 1 & 1 & -1 & -1 & 1 \end{bmatrix} \begin{bmatrix} \frac{\partial p}{\partial x}(0,0,0) \\ \frac{\partial p}{\partial x}(h,0,0) \\ \frac{\partial p}{\partial x}(h,h,0) \\ \frac{\partial p}{\partial x}(0,h,0) \\ \frac{\partial p}{\partial x}(0,0,h) \\ \frac{\partial p}{\partial x}(h,0,h) \\ \frac{\partial p}{\partial x}(h,h,h) \\ \frac{\partial p}{\partial x}(0,h,h) \end{bmatrix},
\tag{B3}
$$

$$
c_2 = \frac{1}{32} \begin{bmatrix} 1 & 1 & -1 & -1 & 1 & 1 & -1 & -1 \end{bmatrix} \begin{bmatrix} \frac{\partial p}{\partial y}(0,0,0) \\ \frac{\partial p}{\partial y}(h,0,0) \\ \frac{\partial p}{\partial y}(h,h,0) \\ \frac{\partial p}{\partial y}(0,h,0) \\ \frac{\partial p}{\partial y}(0,0,h) \\ \frac{\partial p}{\partial y}(h,0,h) \\ \frac{\partial p}{\partial y}(h,h,h) \\ \frac{\partial p}{\partial y}(0,h,h) \end{bmatrix},
\tag{B4}
$$

$$
c_3 = \frac{1}{32} \begin{bmatrix} 1 & 1 & 1 & 1 & -1 & -1 & -1 & -1 \end{bmatrix} \begin{bmatrix} \frac{\partial p}{\partial z}(0,0,0) \\ \frac{\partial p}{\partial z}(h,0,0) \\ \frac{\partial p}{\partial z}(h,h,0) \\ \frac{\partial p}{\partial z}(0,h,0) \\ \frac{\partial p}{\partial z}(0,0,h) \\ \frac{\partial p}{\partial z}(h,0,h) \\ \frac{\partial p}{\partial z}(h,h,h) \\ \frac{\partial p}{\partial z}(0,h,h) \end{bmatrix},
\tag{B5}
$$

where the gradients are calculated based on a finite difference scheme, which needs to include values outside the donor nodes to guarantee third-order accuracy of the interpolation. Here we use a central difference scheme such as

$$
\frac{\partial p(0,0,0)}{\partial x} = \frac{p(h,0,0) - p(-h,0,0)}{2h} + O(\Delta x^2).
\tag{B6}
$$

APPENDIX C: COUPLING THE DISCRETE FORCING TERM WITH PRESSURE-BASED HRR

Guo's forcing term is selected to impose the discrete force [17]. According to the reference, the Bhatnagar-Gross-Krook (BGK) collision model is coupled with the discrete forcing term as follows:

$$
f_i(\boldsymbol{x} + \boldsymbol{c}_i \Delta t, t_n + \Delta t)
$$
$$
= f_i(\boldsymbol{x}, t_n) - \frac{\Delta t}{\tau}[f_i(\boldsymbol{x}, t_n) - f_i^{\text{eq}}(\boldsymbol{x}, t_n)] + \left(1 - \frac{\Delta t}{2\tau}\right) F_i
$$
$$
+ \left(1 - \frac{\Delta t}{2\tau}\right)\Psi_i, \tag{C1}
$$

where the equilibrium function f_i^{eq} is third-order equilibrium function as in Ref. [1]. F_i indicates the discrete forcing term to impose the fictitious force [17], and Ψ_i is the Mach correction term applied in [1]. Macroscopic values (ρ, u and θ) to define the functions f_i^{eq}, F_i, and Ψ_i are calculated based on the definitions of Refs. [1,17]:

$$
\rho \boldsymbol{u}(\boldsymbol{x}, t_n) = \sum_i \boldsymbol{c}_i f_i(\boldsymbol{x}, t_n) + \frac{\Delta t}{2}\boldsymbol{F}(\boldsymbol{x}, t_n), \tag{C2}
$$

$$
\rho(\boldsymbol{x}, t_n) = \sum_i f_i(\boldsymbol{x}, t_n) + \rho(\boldsymbol{x}, t_{n-1})[1 - \theta(\boldsymbol{x}, t_{n-1})]. \tag{C3}
$$

Equation (C1) is arranged as

$$
f_i(\boldsymbol{x} + \boldsymbol{c}_i \Delta t, t_n + \Delta t)
$$
$$
= f_i^{\text{eq}}(\boldsymbol{x}, t_n) + f_i^{\text{neq}}
$$
$$
- \frac{\Delta t}{\tau}\underbrace{\left[f_i(\boldsymbol{x}, t_n) - f_i^{\text{eq}}(\boldsymbol{x}, t_n) + \frac{1}{2}F_i + \frac{1}{2}\Psi_i\right]}_{f_i^{\text{neq}}}
$$
$$
+ \frac{1}{2}F_i + \frac{1}{2}\Psi_i. \tag{C4}
$$

All of the nonequilibrium part f_i^{neq} can be reconstructed through the recursive regularization [27]. The regularization step is conducted through this nonequilibrium tensor such as

$$
a_{\alpha\beta}^{\text{neq},(2)} = \sum_i \left(c_{i\alpha} c_{i\beta} - \delta_{\alpha\beta} c_s^2\right) \underbrace{\left(f_i - f_i^{\text{eq}} + \frac{1}{2}F_i + \frac{1}{2}\Psi_i\right)}_{f_i^{\text{neq}}}, \tag{C5}
$$

and its higher-order moment. More details are provided in Refs. [1,5]. The nonequilibrium tensors reconstruct the nonequilibrium term $\tilde{f}_i^{\text{neq,HRR}}(\boldsymbol{x}, t_n)$, which gives

$$
f_i(\boldsymbol{x} + \boldsymbol{c}_i \Delta t, t_n + \Delta t) = f_i^{\text{eq}}(\boldsymbol{x}, t_n) + \tilde{f}_i^{\text{neq,HRR}}(\boldsymbol{x}, t_n)
$$
$$
- \frac{\Delta t}{\tau}\tilde{f}_i^{\text{neq,HRR}}(\boldsymbol{x}, t_n) + \frac{1}{2}F_i(\boldsymbol{x}, t_n)
$$
$$
+ \frac{1}{2}\Psi_i(\boldsymbol{x}, t_n). \tag{C6}
$$

APPENDIX D: ROTATING AND FIXED GRID COUPLING ALGORITHM

First, we describe the procedure to transfer information from a rotating to a fixed grid. Here the border nodes (receivers) at fixed grid indicate (X, Y) in Fig. 4 (left) (Sec. II D). Eight donor nodes in the rotating grid indicate (x_n, y_n) in Fig. 4 (left) (Sec. II D). Here the number of donor nodes is eight in 3D and four in 2D. The algorithm is described in the 2D case.

Algorithm 1. Interpolation from rotating to fixed grid.

---

for *all border nodes at fixed grid* **do**
    for *4 surrounding interpolating nodes at rotating*
     grid **do**
       $\hat{\boldsymbol{u}}_{mg} = \boldsymbol{u}_{mg} + \boldsymbol{\omega} \times \boldsymbol{r}$;
       interpolation: $\rho_{fg} = I(\rho_{mg})$, $\hat{\boldsymbol{u}}_{fg} = I(\hat{\boldsymbol{u}}_{mg})$,
       $\hat{\boldsymbol{a}}_{fg}^{\text{neq}} = I(\boldsymbol{a}_{mg}^{\text{neq}})$, $\theta_{fg} = I(\theta_{mg})$;
     rotation matrix: $\boldsymbol{u}_{fg} = R(\hat{\boldsymbol{u}}_{fg})$, $\boldsymbol{a}_{fg}^{\text{neq}} = R(\hat{\boldsymbol{a}}_{fg}^{\text{neq}})$;
     reconstruct: $f_{i,fg}^{\text{eq}}, f_{i,fg}^{\text{neq}} = g(\rho_{fg}, \boldsymbol{u}_{fg}, \boldsymbol{a}_{fg}^{\text{neq}}, \theta_{fg})$;

Then the algorithm about passing information from fixed to rotating grids is detailed. The border nodes (receivers) at rotating grid indicate (x, y) in Fig. 4 (right) (Sec. II D). Eight donor nodes in the fixed grid indicate (X_n, Y_n) in Fig. 4 (right) (Sec. II D). Four donor nodes are required in the 2D case, and eight donor nodes are needed in the 3D case, but here we describe only the 2D case. In particular, the last reconstruction step g_{mg} follows the procedure described in Appendix C.

Algorithm 2. Interpolation from fixed to rotating grid.

---

for *all border nodes at rotating grid* **do**
    for *4 surrounding interpolating nodes at fixed grid*
    do
       interpolation: $\rho_{mg} = I(\rho_{fg})$, $\tilde{\boldsymbol{u}}_{mg} = I(\boldsymbol{u}_{fg})$,
       $\tilde{\boldsymbol{a}}_{mg}^{\text{neq}} = I(\boldsymbol{a}_{fg}^{\text{neq}})$, $\theta_{mg} = I(\theta_{fg})$;
     rotation matrix: $\hat{\boldsymbol{u}}_{mg} = R(\tilde{\boldsymbol{u}}_{mg})$,
    $\boldsymbol{a}_{mg}^{\text{neq}} = R(\tilde{\boldsymbol{a}}_{mg}^{\text{neq}})$; $\boldsymbol{u}_{mg} = \hat{\boldsymbol{u}}_{mg} - \boldsymbol{\omega} \times \boldsymbol{r}$;
    reconstruct: $f_{i,mg}^{\text{eq}}, f_{i,mg}^{\text{neq}} = g_{mg}(\rho_{mg}, \boldsymbol{u}_{mg}, \boldsymbol{a}_{mg}^{\text{neq}}, \theta_{mg})$;

APPENDIX E: HIGH MACH ERROR ON THE LBM WITH DISCRETE FORCING TERM: THE CHAPMAN-ENSKOG EXPANSION

Let us expand the LBM equation with a discrete forcing term via the Chapman-Enskog expansion up to the second-order Knudsen number ϵ_2 as Guo *et al.* [17], which reads

$$
\epsilon_0 : f_i^{(0)} = f_i^{\text{eq}},
$$
$$
\epsilon_1 : \left(\frac{\partial}{\partial t_1} + \boldsymbol{c}_i \cdot \boldsymbol{\nabla}_1\right) f_i^{(0)} = -\frac{1}{\tau \Delta t} f_i^{(1)} + F_{1i}, \tag{E1}
$$
$$
\epsilon_2 : \frac{\partial f_i^{(0)}}{\partial t} + \left(1 - \frac{1}{2\tau}\right)\left(\frac{\partial}{\partial t_1} + \boldsymbol{c}_i \cdot \boldsymbol{\nabla}_1\right) f_i^{(1)}
$$
$$
= -\frac{1}{\tau \Delta t} f_i^{(2)} - \frac{\Delta t}{2}\left(\frac{\partial}{\partial t_1} + \boldsymbol{c}_i \cdot \boldsymbol{\nabla}_1\right) F_{1i}. \tag{E2}
$$

Rewrite the first-order Knudsen expansion ϵ_1 of Eq. (E1) in terms of the nonequilibrium part such as

$$f_i^{(1)} = -(\tau \Delta t)\left(\frac{\partial}{\partial t_1} + \boldsymbol{c}_i \cdot \boldsymbol{\nabla}_1\right)f_i^{(0)} + (\tau \Delta t)F_{1i}. \quad \text{(E3)}$$

Take the second-order momentum $\Pi^{(1)} = \Sigma_i \boldsymbol{c}_i \boldsymbol{c}_i f_i^{(1)}$ on Eq. (E3) and follow the algebraic procedure of Hou *et al.* [50], which gives

$$\Pi_{\alpha\beta}^{(1)} = -(\tau \Delta t)\big[c_s^2 \partial_\alpha(\rho u_\beta) + c_s^2 \partial_\beta(\rho u_\alpha) + \partial_{t1}(\rho u_\alpha u_\beta)$$
$$- (u_\alpha F_\beta + u_\beta F_\alpha)\big], \quad \text{(E4)}$$

where the last term comes from the second-order momentum of the discrete forcing term [17]. Also, here we assume that the lattice types are D2Q9 or D3Q19. When we take the second-order momentum $\Sigma_i \boldsymbol{c}_i \boldsymbol{c}_i$ of Eq. (E3), there appears the third-order momentum of the equilibrium function such as $\Sigma_i \boldsymbol{c}_i \boldsymbol{c}_i \boldsymbol{c}_i f_i^{(0)}$, where the type of lattices and the order of equilibrium function bring different results.

The time derivative term $\partial_{t1}(\rho u_\alpha u_\beta)$ can be rephrased by using the momentum and continuity equation as in Ref. [50], which reads

$$\partial_{t1}(\rho u_\alpha u_\beta) = -\partial_\gamma(\rho u_\alpha u_\beta u_\gamma) - \big(c_s^2 u_\beta \partial_\alpha \rho + c_s^2 u_\alpha \partial_\beta \rho\big)$$
$$+ (u_\alpha F_\beta + u_\beta F_\alpha), \quad \text{(E5)}$$

where the last term comes from the Navier-Stokes momentum equation with external force.

Then input the time derivative term into Eq. (E4), which gives

$$\Pi_{\alpha\beta}^{(1)} = -\tau \Delta t c_s^2 \rho(\partial_\alpha u_\beta + \partial_\beta u_\alpha) + \tau \Delta t \partial_\gamma(\rho u_\alpha u_\beta u_\gamma), \quad \text{(E6)}$$

where the last term is the high Mach deviation term. This term can be corrected by projecting it on the second-order Hermite polynomials [30].

In conclusion, according to the Chapman-Enskog analysis, even though there exists the discrete forcing term in the LBM equation, the high Mach correction term maintains the same formulation as the conventional way in fixed inertial reference frame. The necessary condition is the second-order moment of discrete forcing term $\Sigma_i \boldsymbol{c}_i \boldsymbol{c}_i F_i$ has to be $u_\alpha F_\beta + u_\beta F_\alpha$. Guo's forcing term satisfies this necessary condition.

The authors note that the Chapman-Enskogg derivation in this section handles only the $O(u^3)$ high Mach error coming from the lattice defects. Indeed, there exist other error terms in the nonequilibrium tensors, but we do not deal with the other terms because they are composed of scalar values and linear operators which will not be affected by the noninertial frame. More details about the other errors are described in Ref. [51].

[1] G. Farag, S. Zhao, T. Coratger, P. Boivin, G. Chiavassa, and P. Sagaut, A pressure-based regularized lattice-Boltzmann method for the simulation of compressible flows, Phys. Fluids **32**, 066106 (2020).

[2] T. Coratger, G. Farag, S. Zhao, P. Boivin, and P. Sagaut, Large-eddy lattice-Boltzmann modelling of transonic flows, Phys. Fluids **33**, 115112 (2021).

[3] S.-L. Guo, Y.-L. Feng, and P. Sagaut, Improved standard thermal lattice Boltzmann model with hybrid recursive regularization for compressible laminar and turbulent flows, Phys. Fluids **32**, 126108 (2020).

[4] R. Zhang, C. Sun, Y. Li, R. Satti, R. Shock, J. Hoch, and H. Chen, Lattice Boltzmann approach for local reference frames, Comm. Comput. Phys. **9**, 1193 (2011).

[5] H. Yoo, M. L. Bahlali, J. Favier, and P. Sagaut, A hybrid recursive regularized lattice Boltzmann model with overset grids for rotating geometries, Phys. Fluids **33**, 057113 (2021).

[6] J. Favier, A. Revell, and A. Pinelli, A lattice Boltzmann–immersed boundary method to simulate the fluid interaction with moving and slender flexible objects, J. Comput. Phys. **261**, 145 (2014).

[7] I. Cheylan, J. Favier, and P. Sagaut, Immersed boundary conditions for moving objects in turbulent flows with the lattice-Boltzmann method, Phys. Fluids **33**, 095101 (2021).

[8] M. Meldi, E. Vergnault, and P. Sagaut, An arbitrary Lagrangian–Eulerian approach for the simulation of immersed moving solids with Lattice Boltzmann Method, J. Comput. Phys. **235**, 182 (2013).

[9] K. Hejranfar, H. Hashemi Nasab, and M. H. Azampour, Arbitrary Lagrangian-Eulerian unstructured finite-volume lattice-Boltzmann method for computing two-dimensional compressible inviscid flows over moving bodies, Phys. Rev. E **101**, 023308 (2020).

[10] D. Zhou, Z. Lu, and T. Guo, A rotating reference frame-based lattice Boltzmann flux solver for simulation of turbomachinery flows, Int. J. Numer. Methods Fluids **83**, 561 (2017).

[11] M. H. Saadat and I. V. Karlin, Arbitrary Lagrangian–Eulerian formulation of lattice Boltzmann model for compressible flows on unstructured moving meshes, Phys. Fluids **32**, 046105 (2020).

[12] A. Bhadauria, B. Dorschner, and I. Karlin, Lattice Boltzmann method for fluid–structure interaction in compressible flow, Phys. Fluids **33**, 106111 (2021).

[13] E. K. Far, M. Geier, and M. Krafczyk, Simulation of rotating objects in fluids with the cumulant lattice Boltzmann model on sliding meshes, Comput. Math. Appl. **79**, 3 (2020).

[14] P. Lallemand and L.-S. Luo, Lattice Boltzmann equation with overset method for moving objects in two-dimensional flows, J. Comput. Phys. **407**, 109223 (2020).

[15] M. Bahlali, H. Yoo, J. Favier, and P. Sagaut, A lattice Boltzmann direct coupling overset approach for the moving boundary problem, Phys. Fluids **33**, 053607 (2021).

[16] G. Romani and D. Casalino, Rotorcraft blade-vortex interaction noise prediction using the Lattice-Boltzmann method, Aerospace Sci. Tech. **88**, 147 (2019).

[17] Z. Guo, C. Zheng, and B. Shi, Discrete lattice effects on the forcing term in the lattice Boltzmann method, Phys. Rev. E **65**, 046308 (2002).

[18] Y. H. Qian, D. D'Humières, and P. Lallemand, Lattice BGK models for Navier-Stokes equation, Europhys. Lett. **17**, 479 (1992).

[19] T. Krüger, H. Kusumaatmaja, A. Kuzmin, O. Shardt, G. Silva, and E. M. Viggen, *The Lattice Boltzmann Method—Principles and Practice* (Springer, Cham, 2016).

[20] T.-M. Liou and C.-S. Wang, Large eddy simulation of rotating turbulent flows and heat transfer by the lattice Boltzmann method, Phys. Fluids **30**, 015106 (2018).

[21] P. J. Dellar, An interpretation and derivation of the lattice Boltzmann method using Strang splitting, Comput. Math. Appl. **65**, 129 (2013).

[22] G. Silva, Discrete effects on the forcing term for the lattice Boltzmann modeling of steady hydrodynamics, Comput. Fluids **203**, 104537 (2020).

[23] X. He, X. Shan, and G. D. Doolen, Discrete Boltzmann equation model for nonideal gases, Phys. Rev. E **57**, R13 (1998).

[24] Z. Li and X. Shan, Body-force modelling in thermal compressible flows with lattice Boltzmann method, arXiv:2302.04741 [physics.flu-dyn].

[25] K. Suzuki, T. Inamuro, and M. Yoshino, Asymptotic equivalence of forcing terms in the lattice Boltzmann method within second-order accuracy, Phys. Rev. E **102**, 013308 (2020).

[26] J. Latt and B. Chopard, Lattice Boltzmann method with regularized pre-collision distribution functions, Math. Comput. Simul. **72**, 165 (2006).

[27] O. Malaspinas, Increasing stability and accuracy of the lattice Boltzmann scheme: Recursivity and regularization, arXiv:1505.06900 [physics.flu-dyn].

[28] J. Jacob, O. Malaspinas, and P. Sagaut, A new hybrid recursive regularised Bhatnagar–Gross–Krook collision model for lattice Boltzmann method-based large eddy simulation, J. Turbul. **19**, 1051 (2018).

[29] X. Shan, X.-F. Yuan, and H. Chen, Kinetic theory representation of hydrodynamics: A way beyond the Navier–Stokes equation, J. Fluid Mech. **550**, 413 (2006).

[30] Y.-L. Feng, P. Boivin, J. Jacob, and P. Sagaut, Hybrid recursive regularized thermal lattice Boltzmann model for high subsonic compressible flows, J. Comput. Phys. **394**, 82 (2019).

[31] S.-L. Guo, Y.-L. Feng, J. Jacob, F. Renard, and P. Sagaut, An efficient lattice Boltzmann method for compressible aerodynamics on D3Q19 lattice, J. Comput. Phys. **418**, 109570 (2020).

[32] R. Courant, K. Friedrichs, and H. Lewy, On the partial difference equations of mathematical physics, IBM J. Res. Dev. **11**, 215 (1967).

[33] B. van Leer and H. Nishikawa, Towards the ultimate understanding of MUSCL: Pitfalls in achieving third-order accuracy, J. Comput. Phys. **446**, 110640 (2021).

[34] E. F. Toro, *Riemann Solvers and Numerical Methods for Fluid Dynamics* (Springer, Berlin, Heidelberg, 2009).

[35] J. Tölke and M. Krafczyk, Second order interpolation of the flow field in the lattice Boltzmann method, Comput. Math. Appl. **58**, 898 (2009).

[36] X. He, Error analysis for the interpolation-supplemented lattice-Boltzmann equation scheme, Int. J. Mod. Phys. C **08**, 737 (1997).

[37] H. Lamb, *Hydrodynamics*, 6th ed. (Cambridge University Press, Cambridge, 1932).

[38] G. Wissocq, J.-F. Boussuge, and P. Sagaut, Consistent vortex initialization for the athermal lattice Boltzmann method, Phys. Rev. E **101**, 043306 (2020).

[39] M. Geier, A. Greiner, and J. Korvink, Bubble functions for the lattice Boltzmann method and their application to grid refinement, Eur. Phys. J. Spec. Top. **171**, 173 (2009).

[40] O. Inoue and Y. Hattori, Sound generation by shock–vortex interactions, J. Fluid Mech. **380**, 81 (1999).

[41] T. Poinsot and S. Lele, Boundary conditions for direct simulations of compressible viscous flows, J. Comput. Phys. **101**, 104 (1992).

[42] T. Nagata, T. Nonomura, S. Takahashi, Y. Mizuno, and K. Fukuda, Direct numerical simulation of flow past a transversely rotating sphere up to a Reynolds number of 300 in compressible flow, J. Fluid Mech. **857**, 878 (2018).

[43] E. Loth, J. Tyler Daspit, M. Jeong, T. Nagata, and T. Nonomura, Supersonic and hypersonic drag coefficients for a sphere, AIAA J. **59**, 3261 (2021).

[44] M. Gariépy, B. Malouin, J.-Y. Trépanier, and E. Laurendeau, Far-field drag decomposition applied to the drag prediction workshop 5 cases, J. Aircraft **50**, 1822 (2013).

[45] H. Toubin and D. Bailly, Development and application of a new unsteady far-field drag decomposition method, AIAA J. **53**, 3414 (2015).

[46] F. X. Caradonna and C. Y. Tung, Experimental and analytical studies of a model helicopter rotor in hover, Report/Patent Number: NASA-TM-81232 (NASA Ames Research Center Moffett Field, CA, USA, 1981).

[47] B. Vreman, B. Geurts, and H. Kuerten, Large-eddy simulation of the turbulent mixing layer, J. Fluid Mech. **339**, 357 (1997).

[48] S.-G. Cai and P. Sagaut, Explicit wall models for large eddy simulation, Phys. Fluids **33**, 041703 (2021).

[49] G. Wissocq and P. Sagaut, Hydrodynamic limits and numerical errors of isothermal lattice Boltzmann schemes, J. Comput. Phys. **450**, 110858 (2022).

[50] S. Hou, Q. Zou, S. Chen, G. Doolen, and A. C. Cogley, Simulation of cavity flow by the lattice Boltzmann method, J. Comput. Phys. **118**, 329 (1995).

[51] G. Farag, S. Zhao, G. Chiavassa, and P. Boivin, Consistency study of Lattice-Boltzmann schemes macroscopic limit, Phys. Fluids **33**, 037101 (2021).